2011

Structured Silicon Macropore as Anode in Lithium Ion Batteries

Xida Sun
Wright State University

Structured Silicon Macropore as Anode in Lithium Ion Batteries

A thesis submitted in partial fulfillment
of the requirements for the degree of
Master of Science in Engineering

By

Xida Sun
B.E., Heilongjiang Institute of Science and Technology, 2000
M.E., Kunming University of Science and Technology, 2004

2011
Wright State University

WRIGHT STATE UNIVERSITY

SCHOOL OF GRADUATE STUDIES

August 16, 2011

I HEREBY RECOMMEND THAT THE THESIS PREPARED UNDER MY SUPERVISION BY Xida Sun ENTITLED Structured Silicon Macropore as Anode in Lithium Ion Batteries BE ACCEPTED IN PARTIAL FULFILLMENT OF THE REQUIREMENTS FOR THE DEGREE OF Master of Science in Engineering.

Yan Zhuang, Ph.D
Thesis Director

Dr. Kefu Xue, Ph.D.
Chair
Department of Electrical Engineering

College of Engineering and Computer Science

Committee on Final Examination

Yan Zhuang, Ph.D.

Hong Huang, Ph.D.

Kuan-lun Chu, Ph.D.

Andrew Hsu, Ph.D.
Dean,School of Graduate Studies

ABSTRACT

Sun, Xida. M.S.Egr., Department of Electrical Engineering, Wright State University, 2011.
Structured Silicon Macropore as Anode in Lithium Ion Batteries

Porous silicon (PS) membranes for lithium-ion batteries (LIBs) anode applications were developed, demonstrated and characterized systematically in this work. Electrochemical measurements were conducted on both Si-wafer supported and free-standing porous Si membranes. It turned out that the specific capacity of LIBs was enhanced remarkably by PS based anode.

PS was fabricated by using electrochemical anodization in a mixed solution of Dimethylformamide (DMF) and Hydrofluoric acid (HF wt.49%). By varying the anodization conditions, including HF concentration, anodization etching time and current density, pores were formed in a p-type (1-20Ω cm) boron-doped silicon substrate. Scanning electron microscopy (SEM) was employed to investigate the surface morphology of the pores (pore distribution, diameter and depth). The electrochemical agglomeration was observed on the wall of the pores (WOPs). The surface percentage of WOPs was calculated by Finite Element Analysis (OOF2). It turned out that the 27.5 % of the surface is occupied by the WOPs, and the **average** diameters of the pores are in the range between 0.85μm to 1.53μm. The Li insertion in the porous silicon was investigated by cyclic voltammetry method (CV) as well as the small constant current discharge/charge analysis. As increase of the depth of the pores, the specific capacity increased due to the enlarged surface area. The PS anode with 89.4μm of depth showed high cycling stability, manifested by the unchanged porous structure after 10 charge-discharge cycles. The specific capacity up to 1150mAh/g was achieved.

Contents

List of Figures

List of Tables

ACKNOWLEDGMENTS

I would like to thank Department of Electrical Engineering and Department of Mechanical and Materials Engineering at Wright State University for their support of this project.

I would like to express my deepest gratitude to my research advisor, Dr. Yan Zhuang, for guiding me through the research and offering me excellent source of ideas. Besides his tremendous help on my research work, I'm also grateful for his supplies on lab equipments, time and experience at all times. During my last two months working on my thesis, Dr. Zhuang has given me valuable suggestions and broadened my horizon in my research work. He has read and reviewed my manuscript of thesis many times, and given me very useful comments. Without his support and guidance, I would have never been able to complete this thesis.

I am also appreciative to my co-advisor, Dr. Kuan-Lun Chu, who has provided the support, lab and helpful guidance during my research work, and let me have access to top cleanroom, i.e. Nanotech West Laboratory of The Ohio State University. Besides that, he also solved many of the problems we encountered during the course of this research. Without his great assistance and dedicated direct during the completion of this thesis it would never have been completed.

I would also like to thank Dr. Hong Huang, who has given me the great opportunity to do experiments in her lab, her expert guidance in electrochemistry during my research work and very useful comments on my thesis.

I would like to express my appreciation to Dr. Shaurya Prakash and his group for his help in providing the lab to do anodization etching.

I would also like to thank everyone for their nice and kind help. This includes Dr. Paul Steffen, Zhuo Yao, Chuang Guan, Derek Ditmer, Aimee Bross, Karen Bellman, and Li Chen and so on. Last but not least, this work is dedicated to my family, for their love and support under all circumstances.

Chapter 1 Lithium-ion secondary battery

It is well-known that energy is essential to our world as they are closely related with the technological development at present. The Energy Information Administration (EIA) reported that the world's primary energy demand would expand by almost 50% from 2005 to 2030[1]. The internal combustion engine, which consumed about 1/3 of the annual total demand for energy, is a major user of oil. With the concerns about global warming and air pollution, the usage of alternative energy sources, such as nuclear, solar, and wind power, to reduce CO_2 emissions requires devices to store the electric energy generated by these power plants. Currently, more stringent requirements exist both in energy density and power density of energy storage devices in the large applications, such as zero emission electric vehicles and satellites. Batteries are the one of the most obvious solutions to replace the oil for electric vehicle. There is a huge demand for high performance batteries. The lithium-ion battery is a promising option to meet such demands because of its inherent outstanding properties[2]. The ever-increasing demands for energy storage sources with a high energy density has been growing rapidly and calls for the portable computing and telecommunicating equipments required by today's mobile society.

The market for Li-ion batteries (LIBs) has been continuously growing with the fast development of electronic devices as shown in figure 1.1. The production of lithium-ion batteries increases with the demand from the electronics industry.

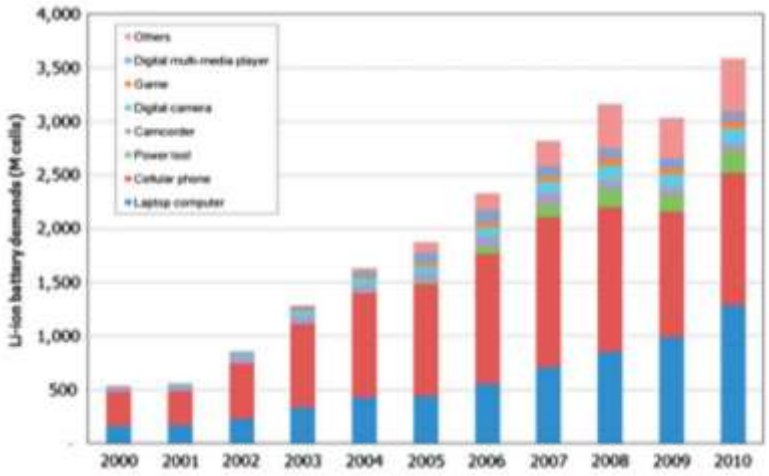

Figure 1.1 Illustration of Lithium-ion batteries market demand [3].

Despite of the dramatic growth in worldwide sales of batteries, the Li-ion batteries technology is often criticized for its slow advancement. Tarascon stated that energy storage limited the development of portable electronic devices and was not able to fit the Moore's law in the computer industry [4]. The conventional materials for batteries have been investigated, reaching the upper limit of capacity of delivering electrical energy [5].

Silicon has the highest specific capacity 4200mAh/g as anode of lithium-ion batteries. However, lithium-ion insertion/extraction process will result in a large volume change (>300%) of silicon anode, leading to the structural pulverization and electrical disconnection from the current collector. As a result, the cell's capacity is decreased with charge/discharge cycling [6]. Nano-structured silicon will play a crucial role in solving these problems and promotes the advancement of renewable energy technologies.

1.1 Brief historical development of Lithium-ion batteries

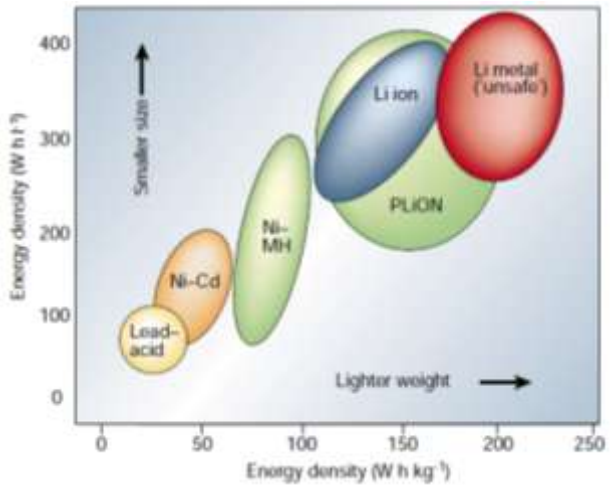

Figure 1.2 Comparison of the energy density among different battery technologies [4]

A battery is generally composed of a cathode (also called positive electrode), an anode (also called negative electrode), and electrolyte. The cathode is the oxidizing electrode which accepts electrons from the external circuit and is reduced during the electrochemical reaction. The anode is the reducing electrode which gives up electrons to the external circuit and is oxidized during the electrochemical reaction. The electrolyte is able to transfer the charge between the anode and cathode.

The reason why Li ion is a promising material as rechargeable batteries is its higher operating voltages, lower self-discharge, no memory effect and high energy density than other materials, the lightest weight 0.534 g/cm^3 at room temperature in the periodic table and the most electropositive metal (–3.04 V versus standard hydrogen electrode). The energy density is compared in **Figure 1.2**[4].

Exxon[8] developed the lithium battery with the TiS_2 as the positive electrode, Li metal as the negative electrode and lithium perchlorate in dioxolane as the electrolyte in

1972. The charging process is the reverse and the cell overall reaction can be written as equation 1.1[9]:

$$Li_xTiS_2 \underset{\text{discharge}}{\overset{\text{charge}}{\rightleftharpoons}} xLi + TiS_2 \quad (1.1)$$

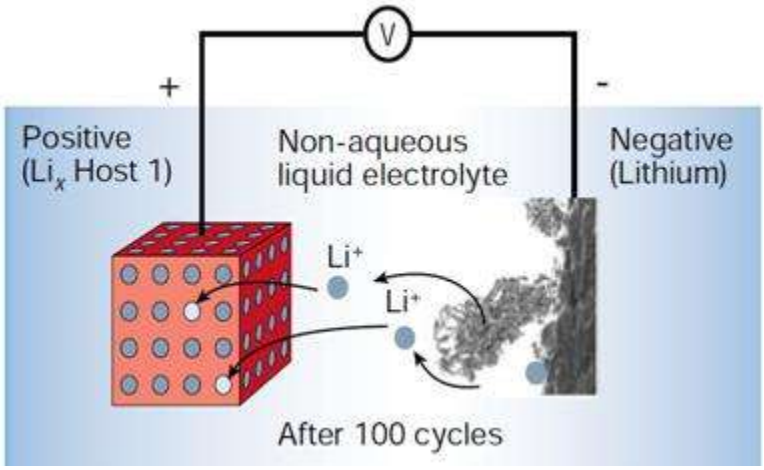

Figure 1.3 Schematic representation of the dendrite growth at the Li surface [4]

The layered structure, intercalation hosts and rigid lattices of TiS_2 can keep the structure of electrode stable during the insertion/extraction of lithium ions. However, the combination between Li-metal and liquid electrolyte can result in a potential explosion due to the dendritic (uneven) Li growth after many discharge–recharge cycles, shown in the **Figure 1.3**.

In order to solve the unsafe issues of the use of Li metal, a family of intercalation materials with a framework structure, which can be used as cathode or anode have been discovered at the end of the 1980s and early 1990s. The negative intercalation electrode is in Li's ionic rather than metallic state, which solved the dendrite problem. In June 1991, Sony Corporation publicly announced the Li-ion battery which was made up of the

carbonaceous material as anode and the $LiCoO_2$ as the cathode. The Li-ion battery had a potential exceeding 3.6 V and gravimetric energy densities as high as 120–150 W h kg^{-1}.

1.2 Principle and structure of Lithium-ion batteries

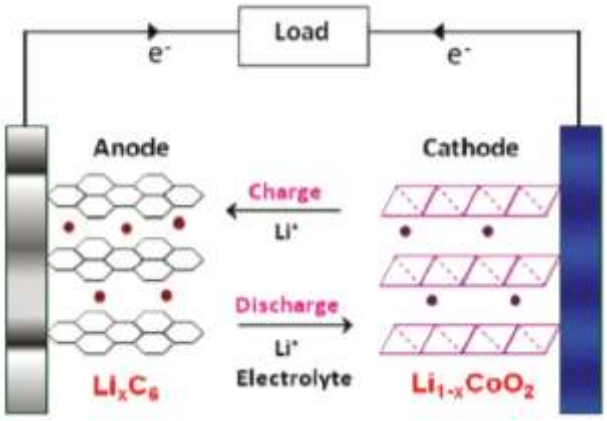

Figure 1.4 Illustration of the charge/discharge process in a lithium ion cell, graphite as the anode and layered $LiCoO_2$ as the cathode.

The operating principles and structure of Lithium-ion batteries are shown in **Figure 1.4**[10]. Lithium ions insert into and extract from anode and cathode during the charge-discharge reversible process [11]. The anode and cathode are electrically insulated by a separator which is porous polypropylene membrane with a host matrix structure.

At present, graphite is the most popular anode material due to its low cost and availability. The graphite shows a theoretical capacity of 372mAh/g to form LiC_6. The intercalation of lithium ions into the graphite structure allows for many repeatable cycles of Li^+ insertions/extraction with little loss in capacity and small volume changes. The passive layers can be formed at the surface of Li-ion battery electrodes, because both anode (such as graphite) and cathode materials for the use in Li-ion batteries are not stable with respect to the electrolyte [17].

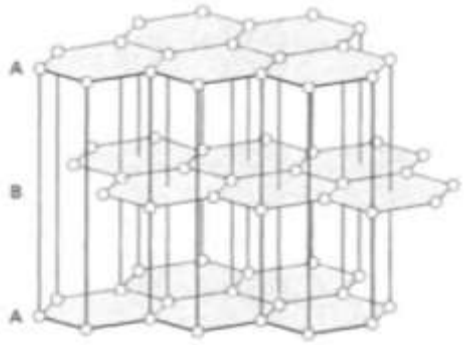

Figure 1.5 Structure of graphite.

The structure of graphite is crystalline, anisotropic and formed by planar layers of carbon atoms stacked graphene layers in an AB sequence, the spacing between planes is 0.335 nm. The volume expansion is about 10% upon Li intercalation.

The cathode material is typically a layered oxide, such as $LiCoO_2$. The electrolyte is generally a mixture of organic carbonates with dissolved lithium salts $LiPF_6$. Ethylene carbonate, dimethyl carbonate and diethyl carbonate are broadly used electrolytes. The battery reaction can be written as follows during charge-discharge cycling [5]:

$$\text{Cathode: } LiCoO_2 \underset{\text{discharge}}{\overset{\text{charge}}{\rightleftharpoons}} Li_{1-x}CoO_2 + xLi^+ + xe^- \quad (1.2)$$

$$\text{Anode: } C_6 + xLi^+ + xe^- \underset{\text{discharge}}{\overset{\text{charge}}{\rightleftharpoons}} Li_xC_6 \quad (1.3)$$

$$\text{Overall: } LiCoO_2 + C \underset{\text{discharge}}{\overset{\text{charge}}{\rightleftharpoons}} Li_{1-x}CoO2 + Li_xC_6 \quad (1.4)$$

1.3 Structured Si-based anodes for Lithium-ion batteries

Anode materials should be pretty active and serve as a host solid into which guest species are reversibly intercalated from an electrolyte [12]. The anodic material, which

can be successfully applied in a rechargeable lithium-ion battery, should have the unique features as follows [12,13].

- High reversible storage capacity for Li and possess long battery life per unit weight or volume of the material;
- Low potential during electrode redox reaction[11];
- The material reacts with lithium in a reversible manner for a lot of charge–discharge cycles;
- The anode' host structure essentially does not change as lithium is intercalated and removed;
- Rapid solid-state Li^+ and electron transport;
- Low cost and environment friendly;
- Reasonable charge/discharge times at room temperature.

Common anode materials in Li-ion batteries include carbonaceous materials, lithium alloy materials, intermetallics, oxides, or silicon[14]. The characteristics of anode materials were shown in the Table 1.1 in comparison with metallic Li.

Table 1.1 Characteristics of anode materials in Li-ion batteries [11,15,16]

Electrode material	**Lithiated Phase**	**Potential Vs. Li (V)**	**Specific capacity (mA·h/g)**	**Volume change (%)**
Li	Li	0 V	3862	100
Graphite	LiC_6	0.1-0.2 V	372	12
Al	LiAl	0.3V	993	96
Titanate	$Li_4Ti_5O_{12}$	1.6 V	175	1
Sn	$Li_{4.4}Sn$	0.6 V	994	260
Si	$Li_{4.4}Si$	0.4 V	4200	320

As can be seen from Table 1.1, Si-based anode is as one of the most promising candidates to replace the conventional graphite anode, because of the high theoretical specific capacity (4200 mAh/g, corresponding to a fully lithiated state of $Li_{21}Si_5$) which is about ten times larger than the specific capacity of graphite (LiC_6, 372 mAh/g). In addition, Li-Si shows low alloying potential versus Li. However, the main challenge for the implementation of Lithium-silicon alloy anodes is the large volume change (up to 300%) during lithium insertion and extraction, resulting in the direct destruction of the initial crystal lattice upon alloying with lithium, severe cracking and pulverization of the electrode, significant capacity loss and bad cyclic performance[24,26].

1.3.1 Silicon-lithium alloy

The Si-based alloy storing Li is different from the intercalation process in that various Li–Si intermetallic phases are formed. Sharma and Seefurth investigated the formation of Li–Si alloys in high temperature cells operating in the 400–500 ˚C range. Their experiments demonstrated that the alloying process in silicon anodes results in the formation of $Li_{12}Si_7$, $Li_{14}Si_6$, $Li_{13}Si_4$, and $Li_{21}Si_5$ alloys [28].

Figure 1.6 shows the Li–Si intermetallic phases in the Li–Si binary phase diagram [22].

The crystalline structures of Li–Si, Si and Li are shown in the Figure **1.7**[29]. When silicon atom accommodates 4.4 lithium atoms, which leads to formation of $Li_{22}Si_5$ alloy, i.e., a specific insertion capacity of 4200 mAh/g, the highest specific capacity among the above alloying elements should be obtained.

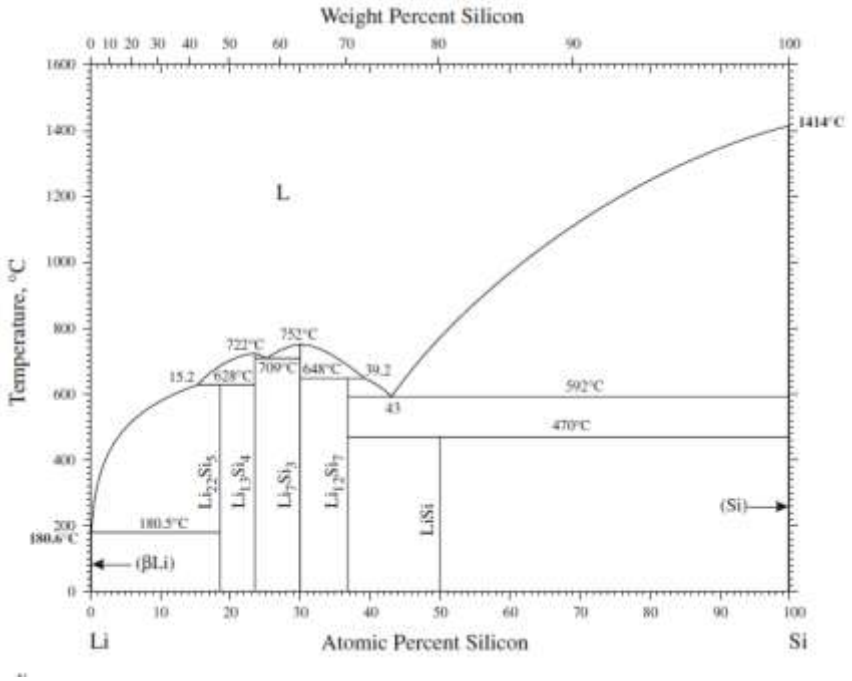

Figure 1.6 The equilibrium phase diagram for the Li–Si system [22].

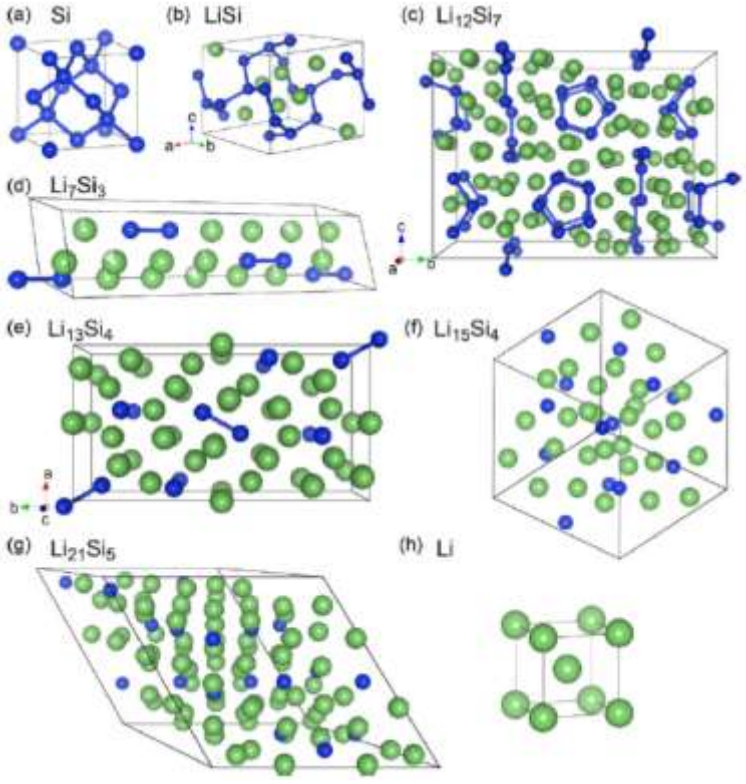

Figure 1.7 Illustration of the crystalline Li–Si structures [29]

The Li-alloying process can be written as the equation 1.5,

$$\text{Li-alloying process:} \qquad Si + 4.4Li^+ + 4.4e^- \underset{\text{discharge}}{\overset{\text{charge}}{\rightleftharpoons}} Li_{4.4}Si \quad (1.5)$$

The calculation of $Li_{4.4}Si$ capacity is shown as follows:

The electric charge of 1 mole electrons is 26764.4 mAh/mol, the standard atomic weight of Si is 28g/mol. The capacity of $Li_{4.4}Si$ is 4205.8mAh/g.

Table **1.2** [28] shows the data for crystal structure, unit cell volume, and volume per silicon atom for each alloy formed during the alloying process. It shows that the volume per silicon atom for $Li_{22}Si_5$ alloy is four times higher than that of the parent silicon atom, i.e., a 400% volume expansion of the silicon lattice occurs theoretically.

Table 1.2 Crystal structure, unit cell volume and volume per Si atom for the Li–Si system[28]

Compound and crystal structure	**Unit cell volume ($Å^3$)**	**Volume per silicon atom ($Å^3$)**
Silicon cubic	160.2	20.0
$Li_{12}Si_7$, ($Li_{1.71}Si$) orthorhombic	243.6	58.0
$Li_{14}Si_6$, ($Li_{1.71}Si$) rhombohedral	308.9	51.5
$Li_{13}Si_4$, ($Li_{3.25}Si$) orthorhombic	538.4	67.3
$Li_{22}Si_5$, ($Li_{4.4}Si$) cubic	659.2	82.4

The advantages and disadvantages associated with the Si-based materials as anode for lithium ion batteries are presented as follows:

Pros:

- High specific capacity.
- Safety characteristics. the thermodynamic potential of lithium alloy formation is 0.4 V vs. Li/Li^+ which reduces the safety and handling problems [23].

Cons:

- The huge volumetric expansion while alloying with lithium. During the formation of Li_xSi_y, the host metal would accommodate x/y moles of lithium ions and the corresponding negative charges. The Si^{x-} ions are larger than the Si^0 atoms. The difference in volume between the lithium-free and the lithiated host is around 300% [23].
- Rapid fade in charge/discharge cycles. The lithium alloys Li_xSi_y host are brittle, which will result in a rapid decay in mechanical stability by mechanical stresses [23].

1.3.2 Mechanism of Li insertion and extraction in Si

During charge–discharge cycling, the structure and morphology change in silicon anodes. According to Kasavajjula and Wang's research work [27], in the process of Li^+ insertion, the crystal structure of Si was destroyed and converted into an amorphous metastable structure without the formation of any intermediate phase at its end 0.0V. High resolution TEM showed that crystalline Si co-existed with amorphous phase [27]. A novel crystalline compound $Li_{15}Si_4$ was formed at a lower potential, but the formation of $Li_{22}Si_5$ was not observed at room temperature. The theoretical capacity of $Li_{15}Si_4$ is 3579 mAh/g. During the extraction, the crystalline $Li_{15}Si_4$ was converted to amorphous lithiated Si with the formation of a two-phase region. At the second Li insertion cycle, amorphous Si was converted to amorphous lithiated Si, the amorphous lithiated Si was converted to the crystalline $Li_{15}Si_4$ phase with the formation of a two-phase region [27]. In the process of Li^+ extraction which is also called recrystallization, the Si anode showed both amorphous and crystalline regions with internal trapping of Li^+ ion at the end of

extraction. In both charged and discharged states, agglomerates of Si particles were found due to Si particles contacted each other [27]. The size of these agglomerates was very large compared with the Si particle. The phase transformation and agglomeration were attributed to poor Li insertion/extraction kinetics, capacity fade, and short cycle life.

1.3.3 Development of microstructured and nanostructured silicon anode

A well-designed microstructure or nanostructure can overcome the detrimental effect of the silicon solid phase volume variations, because of the improvement in its structural, mechanical stability and electrochemical performance during charge/discharge processes. The microstructured or nanostructured silicon performs as buffering the expansions of the silicon solid phase volume variations to accommodate the volume change of silicon and mitigate the mechanical strain and stress, thereby improving the cycle life.

The potential advantages and disadvantages of nanostructured or microstructured materials as anode for lithium-ion batteries as the following [29,30,31,32].

Advantages include:

- The reduced dimensions increase significantly the rate of lithium insertion and removal process, because of the short distances for lithium-ion transport within the particles. The power density is usually reduced by kinetic problems in the electrode materials, i.e., the slow Li^+ and electron diffusion. The characteristic time constant for diffusion is given by $t=L^2/2D$, where L is the diffusion length and D the diffusion constant. Nanostructuring of electrode

materials decrease the value of L, so the time t decreases with the square of the particle size.

- A high surface area permits a high contact area with the electrolyte lead to a high lithium-ion flux across the interface, i.e. higher charge/discharge rates. The composition has often more extensive space for electrolyte and Lithium ions. So the strain associated with lithium insertion/removal is often better accommodated, which should improve cycle life.

Disadvantages include:

- An increase in undesirable electrode and electrolyte reactions due to high surface area, leading to self-discharge, poor cycling, short life and more difficulty maintaining inter-particle contact.
- Nanoparticles may be more difficult to synthesize and their dimensions may be difficult to control.

1.3.3.1 Silicon nanowires as anode

Chan et *al*. prepared the oriented Si nanowires on a steel substrate with the help of gold catalysts via a VLS (vapor-liquid-solid) method [33].The fabricated Si nanowires with average diameter around 89 nm were able to reach up to the theoretical capacity 4,200 mAh/g during this first charging operation as shown in the Figure 1.8 a, b. The Si nanowires, which were doubled in their diameter during the intercalation of Li, withstood more than 10 charging/discharging cycles without a significant loss of capacity and maintain a charge capacity of 75% of its theoretical capacity.

The shortened distance of lithium transport in the silicon nanowires and low-resistance electrical connection also led to the good capability rate (>2100 mAh/g at 1 C) [26]. Although Si nanowires exhibited a higher capacity than other forms of Si, the fabrication process is expensive and not suitable for mass production and commercialization in Li-ion batteries.

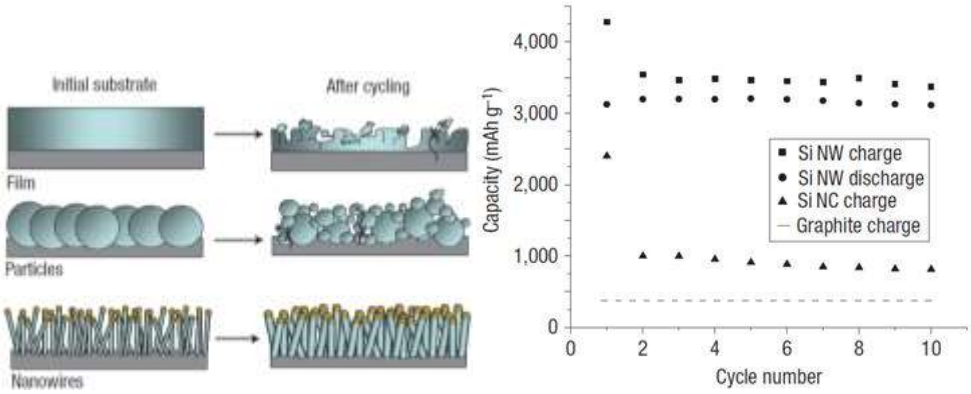

(a) (b)

Figure 1.8 (a) Comparison of conventional Si powders and Si nanowires during charge–discharge cycles (b) Variation in capacity of Si nanowires over 10 cycles [33]

1.3.3.2 Silicon nanotubes as anodes

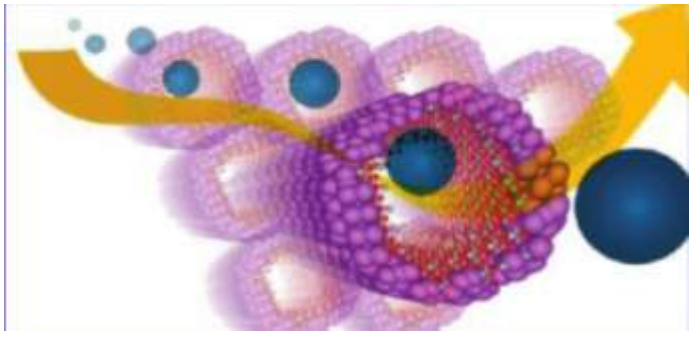

Figure 1.9 Schematic diagram of Li-ion pathway in Si nanotubes [36].

Park et *al*. used a sacrificial alumina template strategy and etching to prepare the Si nanotubes which increased the surface area accessible to the electrolyte and allowed the Li ions to intercalate at the interior and exterior of the nanotubes [36]. The schematic diagram of Si nanotubes is shown in the **Figure 1.9**. The fabricated Si nanotubes showed reversible capacities of 3200 mAh/g (**Figure 1.10** (b)) and capacity retention of 89% after 200 cycles. The Si nanotube morphology is not apparently changed after 200 cycles as shown in the **Figure 1.10** (a). According to the high resolution TEM (HRTEM) analysis [36], the amorphous phase of Si is dominant after reaction with Li.

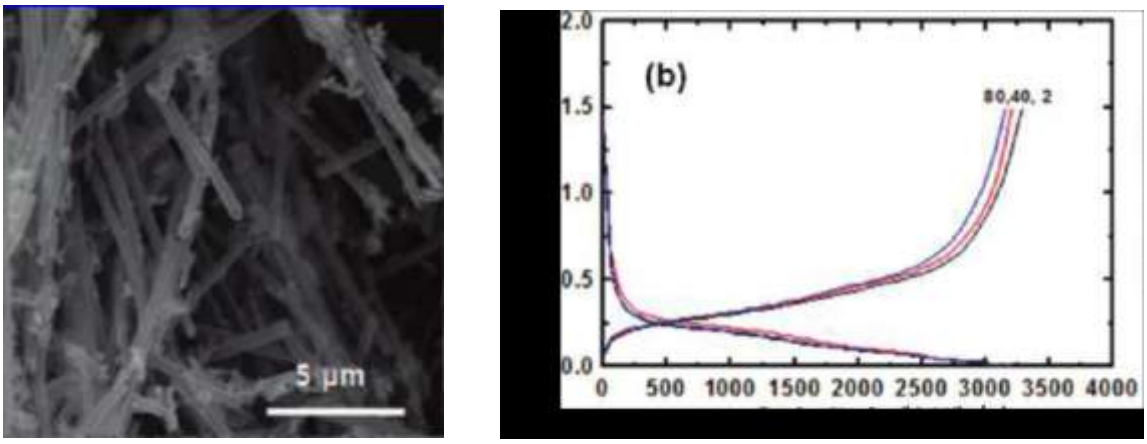

(a) (b)

Figure 1.10 (a) SEM image of cycled Si nanotubes after 200 cycles, (b) Discharge/charge curves after the 2nd, 40th, and 80th cycles [36].

The Si NT arrays can withstand the tremendous stresses and volume changes associated with intercalation of lithium and show the stable cycle retention and reversible morphology change due to the axial void spaces of Si NT.

1.3.3.3 Porous silicon as anode

Shin et *al*. have employed an electrochemical etching method to fabricate porous silicon (PS) which demonstrated the honeycomb-type channels. The specific capacity (/μAh cm^{-2}) of the PS electrodes reached 23 and 85 at 3 CV cycles and 20 CV cycles respectively (**Figure 1.11** c). The channeled structure of the PS electrodes remained essentially the same structure after 35 cycles as shown in the **Figure 1.11**(a,b), in spite of the severe deformation of the channel wall during the repetitive lithium insertion/extraction process [37]. The channel wall of the PS participates in the lithiation/delithiation process, which has been confirmed by Shin.

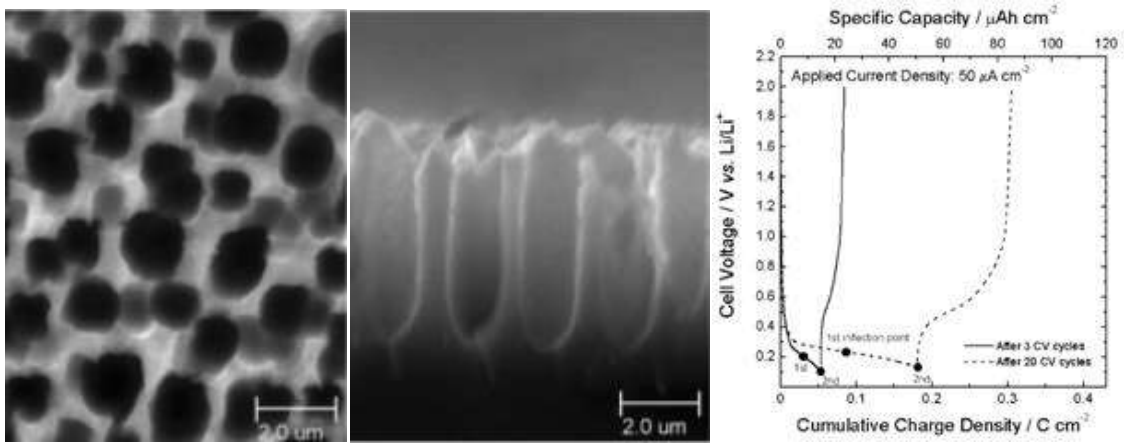

(a) (b) (c)

Figure 1.11 The morphological change of the porous silicon anodes 35 cycles, (a) top view, (b) cross-sectional view, (c) voltage profiles of the PS samples after 3 and 20 CV cycles.

1.4 Summary

Recently, the huge necessity for energy storage sources with a high energy density has been growing rapidly. However, the progress of Li-ion batteries technology was hindered by the delaying developments of electrode material. Si-based materials is considered to be an ideal anode replacement for Li-ion batteries because of its large lithium storage, however, the wide usage was restricted due to its dramatic volume

expansion and contraction during Li insertion and extraction [14]. The volume change, which results from the lattice's stress, cracking and crumbling of the alloy particles during cycling, leads to the pulverization of the electrode materials, poor cyclic performance and abrupt loss in capacity within a few charge-discharge cycles. A well-designed microstructure or nanostructure can overcome the detrimental effect of the silicon solid phase volume variations, because of the improvement on its structural, mechanical stability and electrochemical performance during charge/discharge processes.

In this work, we try to improve the performance of Lithium-ion batteries by applying a novel porous Si membrane as the anode. The entire research work includes the fabrication and morphological characterizations of porous silicon membranes, and electrochemical analysis of the novel porous structures of Si working in the half-cell configuration. The current researches on micro- or nano-structured materials as anode in LIBs, and fabrication as well as formation mechanism of porous silicon are reviewed in chapter 1 and chapter 2. In chapter 3, the experiment of macroporous silicon fabrication is implemented, and the morphology of this kind of porous Si structure is investigated by SEM and OOF2 finite element analysis software. The experimental apparatus, cell preparation, battery testing procedures and analysis of experimental results are described in chapter 4. The conclusion of the thesis work and future work are discussed in the chapter 5. The results of SEM images and the calculation for pore morphology are shown in the Appendix.

Chapter 2 The Porous Silicon

Silicon has been recognized as the most important material of miniaturized mechanical and electrical devices and components due to its role of being used as substrate in integrated circuits, like sensors and transducers [41]. In Earth's crust, silicon is the second most abundant elements, making up about 27.7% of the crust's mass [42]. The technique of silicon based micromachining is more mature than other materials at present, resulting in silicon as the most promising material for micromachining.

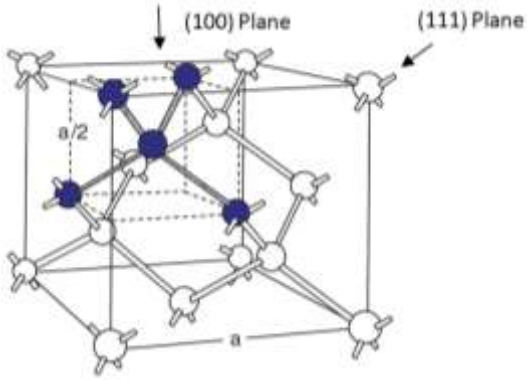

Figure 2.1 Valence-bond model of the silicon crystal. Dark atoms define the unit cell. Lattice constant a = 0.54307nm

The silicon crystal cell consists of eight atoms connected together by 16 covalent bonds with a native diamond structure. Three dimensional representation of the silicon crystal is shown in the Figure 2.1. In this model, the covalent bond between two adjacent atoms was come into being by two valence electrons. The energy required to break the single covalent bond Si–Si at zero temperature , 1 atm (101,325 Pa) is 4.63 eV [43].

2.1 Category of Porous Silicon

Porous silicon is a very promising material due to its large surface area within a small volume and inherent properties of silicon. Porous silicon (PS) was first observed in electropolishing adopting a current density for a given HF concentration by Uhlir in 1956[19]. He found that the Si wafer was dissolved partially in case of a current below a certain threshold. In addition, the pore size is reproducible and controllable, and the processing of porous silicon is compatible with silicon-based microelectronics, ensuring mass production and low cost.

In general, PS is introduced by electrochemical anodic etching in an HF based solution, named anodization[38]. International Union of Pure and Applied Chemistry (IUPAC) categorized the porous silicon into three categories as exhibited in Table 2.1 [39].

Table 2.1 Category of Porous Silicon

Name	Pore diameters and Pore distances
Micropore	<10 nm.
Mesopore	10–50 nm
Macropore	>50 nm

The three species of pores can be fabricated under diverse conditions with unlike morphologies [40], addressed in **Figure 2.2**. The key parameters are the chemical formula of the electrolyte (organic or non-organic), the HF concentration and the doping type of the Si. In most situations, the disparate illumination condition (back or front), can result in morphological transformation as well.

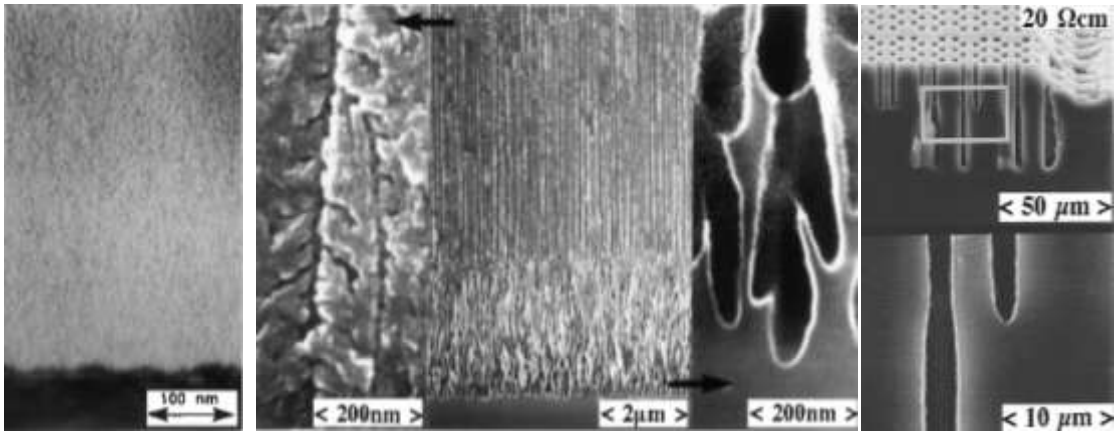

(a) (b) (c)

Figure 2.2 SEM image of PS, (a) cross-sectional view of micropore formed at p-type substrate, 100 mA cm^{-2}in 1: 1 ethanoic HF,(b) cross-sectional view of mesopore formed at 300 m A cm^{-2}, n-type in ethanoic HF, (c) cross-sectional view of macropore formed at 5m A cm^{-2}, n-type substrute in 2.5% HF[51].

2.2 Electrochemical dissolution of silicon in HF based solution

Electrochemical etching of silicon is obtained by applying electrical current (I) in a given electrolyte. When a voltage is applied from a power supply between the Si wafer and the counter electrode, the current will pass through the Si wafer. In most cases, the backside of Si wafer needs to be coated with a conducting layer. A platinum electrode serves as counter electrode.

Usually the etching process involves in charge transfer. Under the scenarios of low current densities and high concentrated HF solution, the porous silicon (PS) can be acquired.

Holes can be offered by an electrochemical circuit. The electrochemical dissolution of Si in HF based solution requires two positive charged holes to remove one silicon atom from the surface of the silicon. In the following two-step process (Equation 2.3.1) and (Equation 2.3.2), are described. The holes can be supplied by the voltage

source. At the same time the H_2 bubbles will be shaped, and the silicon surface will then be oxidized [42].

$$Si + 2h^+ + 2H^+ \rightarrow Si^{4+} + H_2 \qquad (2.3.1)$$

$$Si^{4+} + 6HF \rightarrow SiF_6^{2-} + 6H^+ \qquad (2.3.2)$$

The Reaction mechanism for silicon dissolution in HF-based solutions can be seen in Figure **2.3**. The Si dissolution rate is zero at open circuit potential (OCP) [46].

After a hole from the bulk approaches to the interface between silicon and electrolyte, the Si-H bond is attacked by a fluoride ion (step 1, Figure **2.3**). The HF or HF_2^- is the reactant that is easy to share electrons to other molecules in the course of chemical reaction [52]. After one Si–F bond is established, another Si-H bond is attacked, and gaseous H_2 occurs (step 2 and step 3, Figure **2.3**).

The $Si_2{=\!=\!=}Si{=\!=\!=}F_2$ is continuously attacked by one HF_2^- ions (step 4, Figure **2.3**). Finally, surface silicon atoms are changed into SiF_4 and dissolved as SiF_6^{2-} ions (step 5, Figure **2.3**).

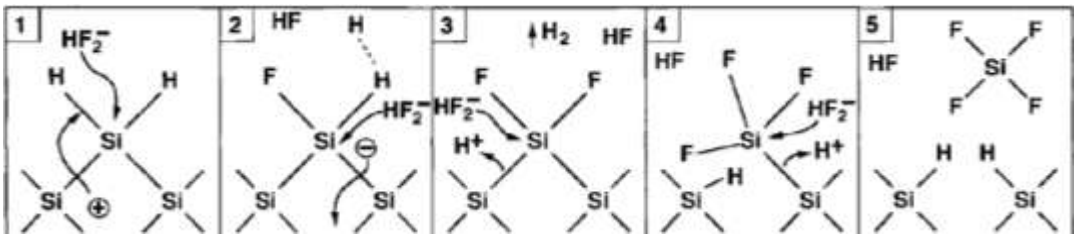

Figure 2.3 Illustration of the electrochemical dissolution of silicon [46]

2.3 The macroporous silicon

Macroporous silicon is produced in a hydrofluoric acid (HF) based solution with the silicon wafer as the anode and the platinum as the cathode. The whole system is

immersed in a teflon beaker filled with the HF based solution (Figure **2.4**). When a current flows through the solution and the silicon wafer, the electrochemical reaction occurs and generates the small pits on the surface of silicon. The chance of further removal of Si from the pits is greater than that from the surrounding area. The formation of porous silicon is able to continue until the current is reduced below the critical point. Holes facilitate the oxidation processes for pore formation [53], so p-type silicon is easy to make porous silicon. Parameters which are responsible for the morphology of porous silicon include current density, HF concentration, and doping type of the silicon substrate.

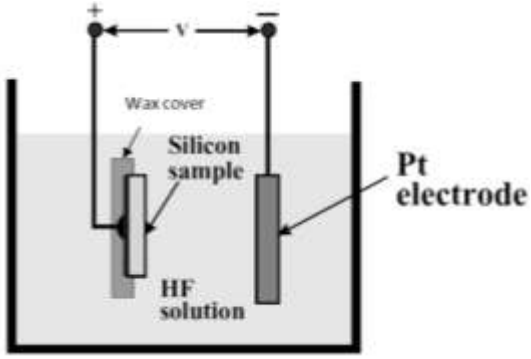

Figure 2.4 Basic process set-up for porous silicon formation.

2.3.1 Macropore's formation in n-type silicon

Macropores in n-type silicon acquired with organic electrolytes and back side illumination was reported in 2000 [55]. Illumination instead of applied bias should have an impact on the pore tip current [46]. Although electronic holes are in short supply in n-type silicon, the illumination of the electrode, which is the source of holes, generates the flux of holes needed for the dissolution process (Figure **2.5** a). The SEM image of fabricated macropore is found in the Figure **2.5** b.

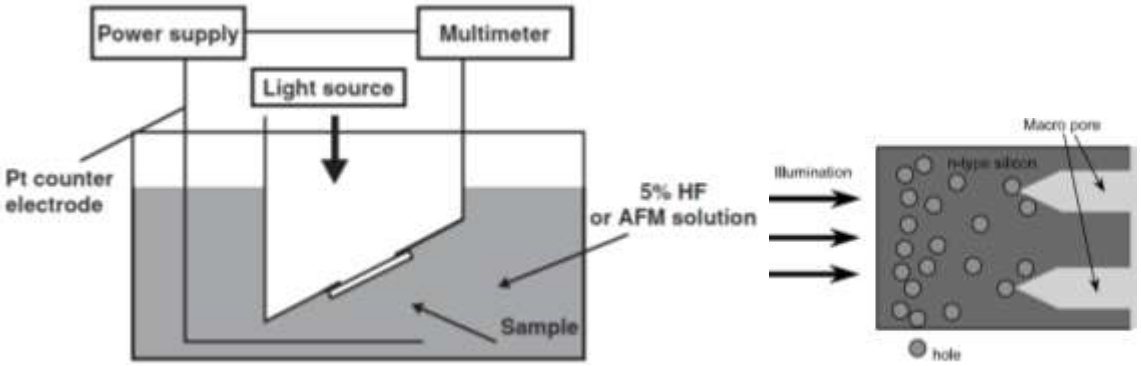

(a)

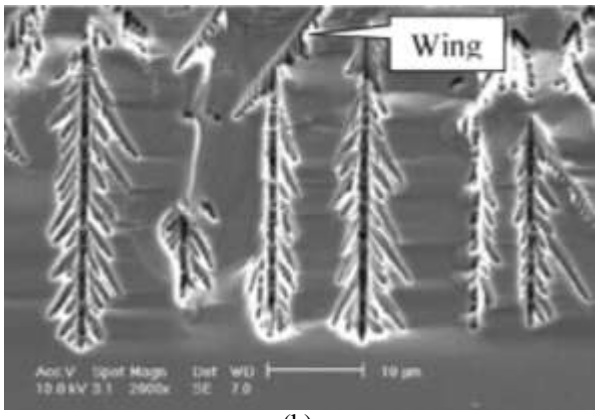

(b)

Figure 2.5 Illumination of macropore by n-type silicon, (a)Set-up for the macroporous formation in n-type silicon[40], (b)SEM image of n-macropores at 2 mA/cm^2[4].

2.3.2 Macropore's formation of p-type silicon in organic solution

Propst and Kohl discovered the fabrication methods for p-type silicon macropores in organic solution in 1994[56]. The (1 0 0) oriented p-type macroporous silicon can be formed by the HF (wt. 49%) plus organic solutions under forward scenes, the organic solutions include acetonitrile (MeCN), propylene carbonate (PC), dimethylsulfoxide (DMSO) and dimethylformamide (DMF) [39,57].

In DMF and DMSO, macropores have been engendered in p-Si with resistivity down to 0.2 Ω cm [58]. Later, the group of Kohl performed the experiment that the electrochemical etching of silicon in anhydrous HF solution plus acetonitrile (ACN), no macroporous silicon was retrieved for p-type silicon, it was significant that the small amount of water which is provided by HF (wt.49%) control the formation of porous silicon [59].

The critical current density peak of i-V characteristics does not occur in organic electrolyte for the formation of macropore of silicon due to the large resistance of the organic electrolytes[46]. In contrast to n-type macropores, backside illumination is unnecesary, easy to make.

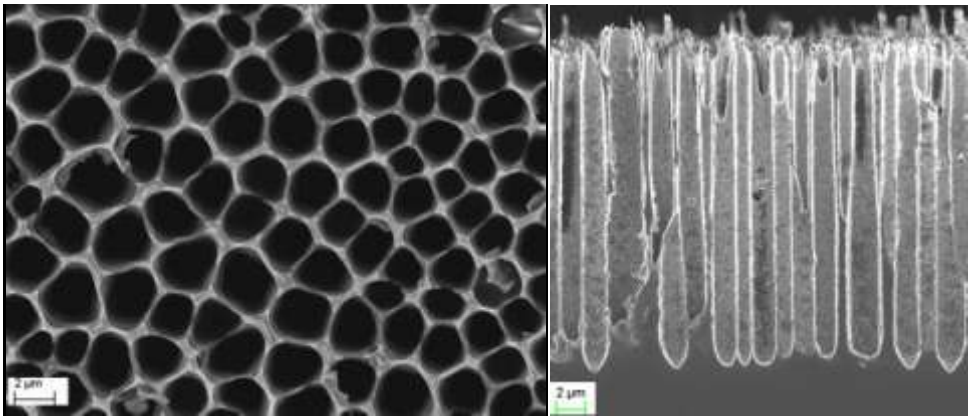

(a) (b)

Figure 2.6 SEM images of electrochemically etched p-Si(1 0 0) in 4 M HF + DMF, (a) tope view, (b) cross-sectional view.

2.4 Macropore formation mechanisms in p-Type Silicon

In order to construct pore structure, the dissolution rate at the pore tip should be higher than at the side wall. Lehmann et al. considered that macropore formation on p-type substrates can be understood as a consequence of the charge-transfer mechanisms in

a Schottky diode under forward conditions, i.e. a metal-semiconductor contact [60]. The silicon dissolution is controlled by the charge transfer with the flow of holes overcoming a Schottky barrier under weak depletion conditions and reaching the surface. The basic charge distribution around pores in a p-type electrode is shown in Figure 2.7. The space-charge region is present near the interface between the solution and the macropore.

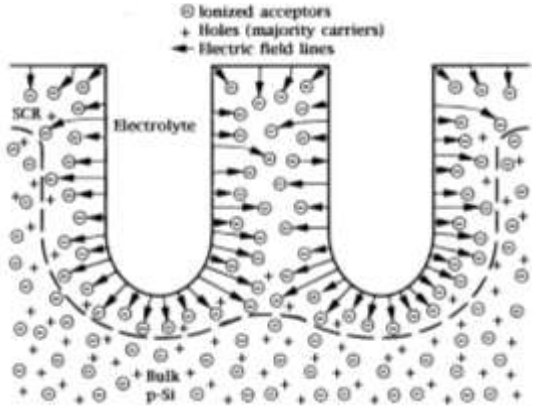

Figure 2.7 The basic charge distribution around pores in a p-type electrode [46].

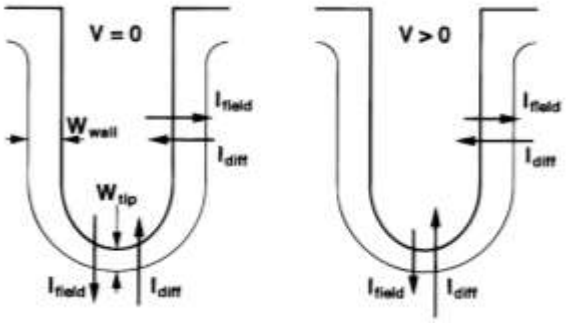

Figure 2.8 Relationship among the diffusion current, drift current and the forward bias [60].

There are two sorts of current density, one arising from diffusion of charge carriers, another originating from the drift of charge carriers. Under forward conditions during macropore formation, the diffusion current is bigger than the drift current as can be seen in Figure **2.8**, the overall rate of hole transfer is proportional to the total current

density $I_{total}= (I_{diff} - I_{drift})$. This quantity I_{total} is inversely proportional to the width of the space-charge region of Schottky diode which is thinner at the tips than at the sidewall. Hereby the dissolution rate is higher due to the higher diffusion velocity of hole at macropore tips [46]. According to these ideas, the wall thickness is determined by the thickness of the width of the space-charge region. The maximum thickness of pore wall is just 2 folds of the width of space-charge region. The space-charge region should be influenced by the p-type doping density and the applied potential.

2.5 Summary

Table 2.2 The parameter which affects the formation of porous silicon

Parameter	Remarks
Voltage and current	There are two methods, one is potentiostatic method (the voltage V is given and the current I adjusts), another is galvanostatic method (the current I is given and the voltage V adjusts). Galvanostatic method usually can get the repeatable formation of porous silicon.
The HF concentration	The HF concentration can determine the etch rate [61].
The doping type, density and level	The applied potential increases with the doping level. High doping levels reduce the ability to form macropores and increase the etch rates due to enhanced injection of holes in the case of p-type silicon in organic solution [39]. For n-type wafers the etch rate can be affected by the doping level, since holes are provided by illumination. The macropore densities N_p increase linearly with doping density[46].
The solvent added to the HF solution	H_2O, Ethanol (EtOH), other alcohols, organic solvents like DMSO, DMF and Acetronitrile.
The etching time	The depth of pore increase with the etching time.
The current density	The etch rate increase with the current density.
The illumination during the etch	It is necessary for n-type silicon.
Temperature	Generally better results at low temperatures between room temperature to -40 °C[61].

There is an amount of choice of electrolytes and etching conditions with respect to pore formation, but it is hard to predict it. So the formation of the well-designed pores is a process of empirical optimization [61]. The parameters that determine or influence the pore properties are expressed in the table 2.2.

Chapter 3 Experimental results and discussions of macroporous silicon

3.1 Fabrication of porous silicon

3.1.1 Selection of silicon wafer

Boron-doped (p-type), single-side polished, and (100) oriented 4" silicon wafers with an electrical resistivity of 1-20Ω cm were used as the substrate. The thickness of the substrate is 375 ± 25 μm with a *total thickness variation (TTV), i.e.* the difference between the minimum and maximum thickness should be less than 10 μm.

3.1.2 Backside protection

The metal layer on the backside of the silicon wafer was covered by the SU-8 photoresist to prevent unnecessary electrochemical etching in the HF based solution. The completed wafer with the coated Au and photoresist is shown in the figure 3.1(a).

SU-8 2005 was firstly coated by utilizing a spin coater at 1000rpm without a pretreatment, and later baked on a hotplate at 95˚C for 3 minutes. The wafer was then cut into a rectangular shape. To get a good estimation of the current density, the open area is defined either in circular or rectangular shape by covering the acid-proof wax around the edge, as shown in figure 3.1 (b).

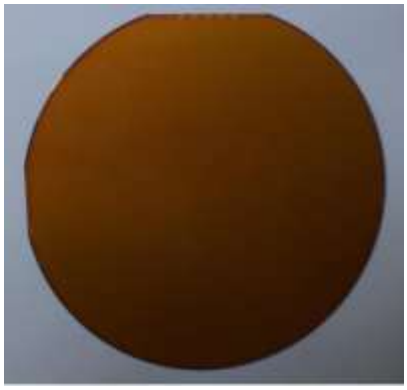

(a)

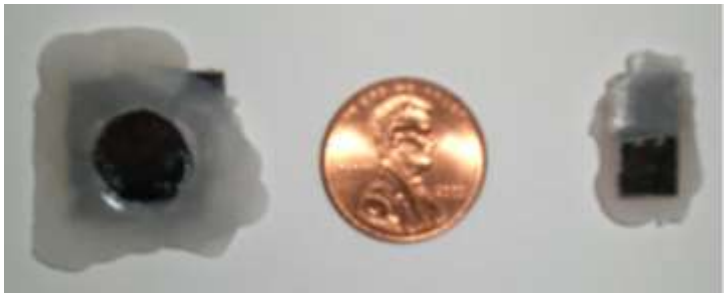

(b)

Figure 3.1 (a) The completed whole wafer with coated Au and Photoresist, (b) samples for electrochemical etching

3.1.3 Chemical solution for electrochemical etching

The solution for the electrochemical anodization etching consists of the Hydrofluoric acid (HF wt 49%) and pure DMF(N,N-Dimethylformamide) with various concentrations. DMF is an organic compound with a molecular formula of $(CH_3)_2NC(O)H$ and can co-mix with water in all proportions. The Hydrofluoric acid (HF 49%) is extremely corrosive colorless acid, so the experiment must be operated in the chemical hood for safety. The experimental conditions are illustrated as Table 3.1.

Table 3.1 Various concentrations of DMF and HF for fabrication of Porous silicon.

Electrolyte	HF wt.49% (ml)	DMF (ml)
1M HF	8.25	192.75
2M HF	14.49	185.51
3M HF	21.74	178.26
4M HF	28.99	171.01

The procedure for the fabrication of the porous silicon samples is based on the method reported by Ponomarev [57], who demonstrated a basic description of electrochemical anodisation using a HF plus dimethylformamide (DMF) mixed solution to get the silicon macropore.

This electrochemical etching resulted from either the anodic constant current or potential. The porosity, thickness and a good reproducibility obtained by constant current were more controllable than by constant potential from run to run[45].

In this work, a more detailed investigation on the morphology of macroporous silicon has been demonstrated under the condition of using different parameters i.e. current density, etching time and HF concentration in the electrochemical anodisation system at room temperature shown in figure 3.2. The cell body is PFA Griffin Beaker made of highly acid-resistant Teflon resin by Nalgene. The silicon wafer is cut into rectangular or triangular pieces, and connected to positive electrode of power supply serving as the anode. The cathode is made of platinum wire which is HF-resistant and conducting material. The platinum wire was connected to negative electrode of power supply and winded as circle plane shape. Agitation is provided by an electric stirrer equipped with a polyethylene paddle.

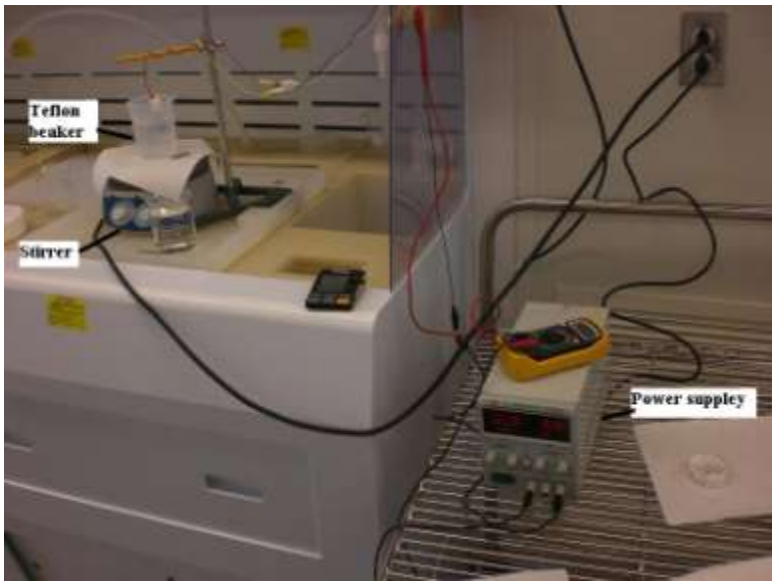

(a)

(b)

Figure 3.2 The experiment set-up for porous silicon fabrication (a) setup overview; (b) Porous silicon fabricated in the Teflon beaker

Porous silicon was created on the open area with direct contact with the HF solution. The etching time, HF concentration and current density will affect the morphology of porous silicon. A number of tests with different conditions as shown in table 3.2 were carried out to find the impacts on the morphology of porous silicon, such as depth and diameter of pore.

Table 3.2 Condition parameters for fabrication of porous silicon.

Sample	HF concentration (M/L)	Current density (mA/cm^2)	Etching time (minutes)
4M01	4	10	10
4M02	4	10	20
4M03	4	10	30
4M04	4	20	10
4M05	4	20	20
4M06	4	20	30
4M07	4	30	10
4M08	4	30	20
4M09	4	30	30
4M10	4	40	10
4M11	4	40	20
4M12	4	40	30
4M13	4	40	40
4M14	4	40	55
4M1019	4	50	30
4M1021	4	50	60
3M01	3	10	20
3M02	3	20	20
3M03	3	30	20
2M01	2	10	20
2M02	2	20	20
2M03	2	30	20
1M01	1	10	20
1M02	1	20	20
1M03	1	30	20

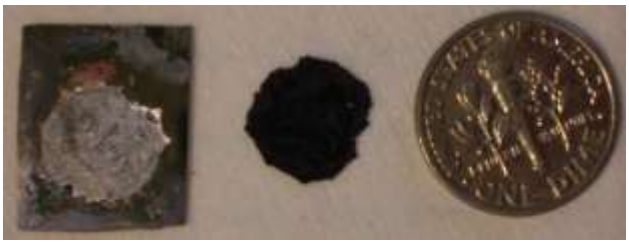

Figure 3.3 Image of free-standing PS film (middle one), Silicon substrate (left)

Figure 3.4 Image of free-standing PS thin film with coated copper (middle), Silicon substrate with coated copper (left).

Take the 4 M HF solution as an example, the free-standing porous silicon film can be obtained by the following procedure (table 3.3):

Table 3.3 Procedure of fabrication for free-standing silicon macropore

No.	Description
1	Begin with wax protected Si wafer piece.
2	Preparation of the 4 M HF solution 200mL, which need pour slowly 171 mL DMF into 33.3g HF (wt. 49%) in 250mL PFA beaker.
3	Using banana plugs to connect the DC power supply (HY3005D), the positive(+) terminal in the power supply should connect with silicon wafer piece, the negative terminal (-) in the power supply should connect with the coil of platinum wire.
4	Using stand to loop electrical wires around for hanging the silicon wafer piece and the coil of platinum wire.
5	Put the platinum coil close to silicon surface. Lower wafer piece and the platinum coil until the solution just covers etching area but does not touch the banana plug ends.
6	Turn on power supply, in order to get the current 40mA, we need increase the voltage from zero to around 14.4V to 17V. The etching should last one hour
7	Increase the voltage to 32.2 V after step 6.
8	Leave for 10-12 minutes, the porous silicon usually can be peeled off from the silicon substrate.
9	The fabricated free-standing PS is shown in the Figure 3.3.

In order to improve the conductivity of the free-standing macropore, a layer of copper is evaporated on the surface of macropore thin film (Figure 3.4). Due to that the free-standing macropore thin film is very fragile, a silicon substrate should work as the support which sticks the edge of the macropore thin film by photoresist. When the evaporation being accomplished, acetone was applied to dissolve the photoresist and left a whole free-standing macroporous silicon thin film with a copper layer. The thickness of the Cu thin film is approximately 18nm or 115nm corresponding to a growth rate of 0.1Å-0.2Å per second.

3.2 Estimation of the diameter, wall-width, and density of the macropores

In this work, the area percentage of pore should be calculated by the software-namely, Finite Element Analysis of Microstructures (OOF2 version), on the basis of finite element analysis of microstructure, the macroscopic properties can be gained by the images of real microstructures. The Ubuntu Linux system was executed for the running of OOF2.

3.2.1 The number of the pores in the SEM image

The number of pores within a specific area N_{pore} = horizontal number × vertical number. The horizontal and vertical number of pores was averaged over three horizontal and vertical cross lines on a SEM image, respectively.

3.2.2 The area of the pores on a SEM image.

The area percentage of pore is estimated by using OOF2, i.e. the pixels of pore divided by the pixels of the total area. Uploading the top view of SEM image, the area of the pores can be recognized by a gray value of the point selected with the value 0.076 as delta_gray parameter. OOF2 should mark the area as the red color, if the difference in gray value between selected color and the color of any part in the image is less than 0.076, the part would be chosen as the area of pore. The value of delta_gray parameter is a real number in the range [0, 1], where 0 indicates no intensity difference, and 1 indicates the maximum possible difference. It specifies the difference between two colors by converting them to grayscale, and comparing the results. The difference between two colors is less than Delta Gray, the area would be selected [7]. The red color region is the area of pore shown in the figure 3.6 (b).

The area of the pores A_p= total area of the SEM image A_t × area percentage of pore.

3.2.3 The average diameter of the pores d

The average diameter of the pores $d = 2 \times \sqrt{\frac{A_p}{N_{pore} \times \pi}}$

Where A_p is the area of the pores, N_{pore} is the number of the pores.

3.2.4 The average width of pore wall W

Assuming that the pores locate in the center of the square are uniform distributed as the figure 3.5, the W represents the width of wall, D represents the length of side.

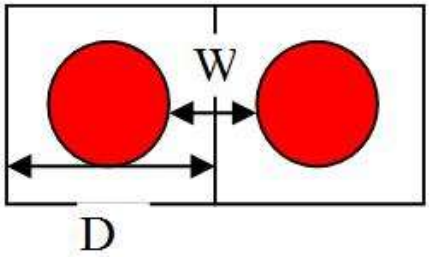

Figure 3.5 The model of illustration of pore distribution and size

The average width of pore wall:

W= the length of side of the square D− the average diameter of the pores d.

Where $D = \sqrt{\frac{A_t}{N_{pore}}}$

3.2.4 The calculation of d, D and W of pore

Take the sample 1M02 as an example, the area of SEM image (Figure 3.6 (a)) is 1022× 674 pixels, the red color region is 370049 pixels (Figure 3.6 (b)), the area percentage of pore for the 1M02 is,

$$\frac{370049}{1022 \times 674} \times 100\% = 53.7\%$$

The number of the pores N_{pore} in the SEM image of 1M02 is 35 ,see figure 3.6 (a).

The total area of the SEM image $A_t = \frac{\text{the lenth} \times \text{the width of image}}{\text{the scale}^2} = 39\ \mu m^2$

The area of the pores $A_p = At \times 53.7\%$

The average diameter of the pores $d = 2 \times \sqrt{\frac{A_p}{35 \times \pi}} = 0.873 \mu m$

The length of side of the square $D = \sqrt{\frac{A_t}{N_{pore}}} = 1.056 \mu m$

The average width of pore wall W= D – d= 0.183μm

The pore density $N_p = \frac{N_{pore}}{A_t} = 0.897\ /\mu m^2$

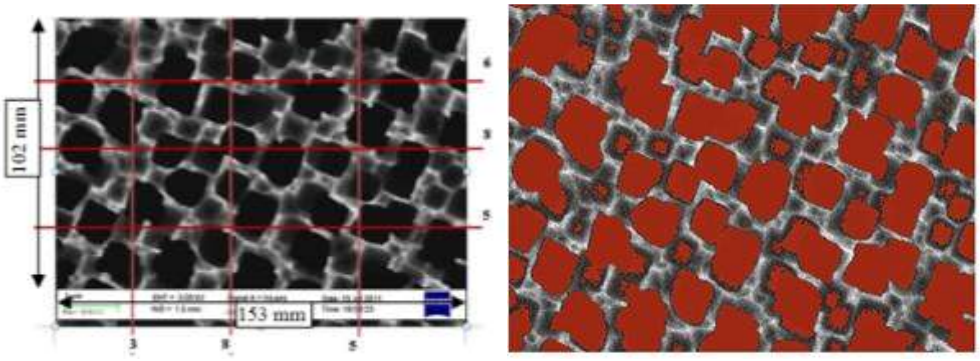

(a) (b)

Figure 3.6 The SEM image of 1M02, (a) before;
(b) after calculation of pixel by OOF2

The summarized calculation results of the diameter, wall-width, and density of the macropores were presented in the Appendix.

3.3 Results

3.3.1 Pore diameter d, pore density N_p , width of pore's wall W, and deth of the pore

The pore diameter d, pore density N_p and width of pore's wall W are calculated by the method mentioned in the section 3.2, the summarized results are indicated in the Appendix.

Observed from figure 3.5, the average diameters of the pores are 0.873μm, 0.919μm, 0.850μm and 1.526μm at 1M, 2M, 3M and 4M HF solution respectively, when the current density is 20 mA/cm^2. Increasing the current density to 30mA/cm^2, the

average diameters of the pores are 1.214μm, 1.043μm, 1.197μm and 1.121μm at the 1M, 2M, 3M and 4M HF solution respectively. From our experiments, it is still obscure how the average diameter depends on the HF concentration and current density. For various HF concentrations and current densities, the average diameters of the pores are in the range between 0.85 μm to 1.53 μm.

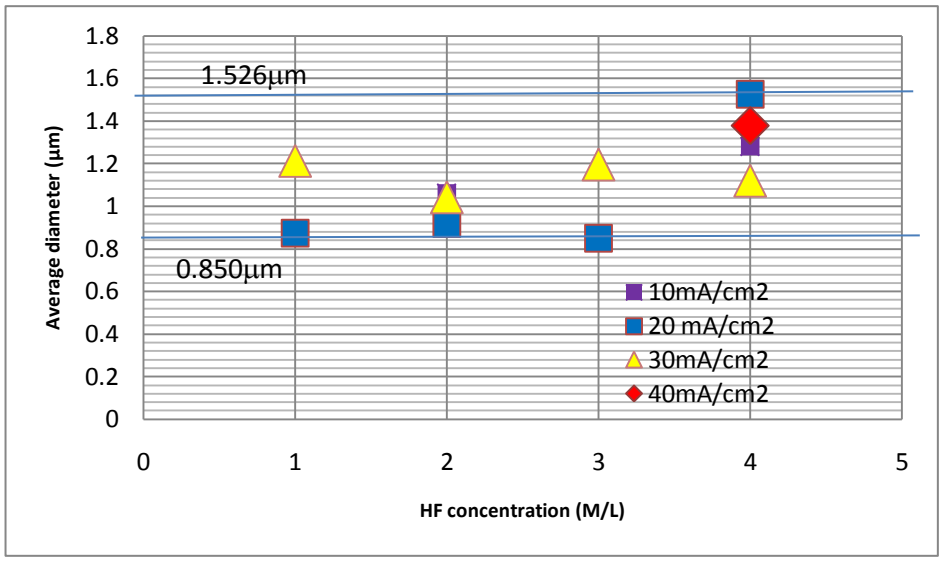

Figure 3.7 The variation of average diameter with different HF concentrations and current densities. The etching time is 20 minutes.

As can be seen from figure 3.8, the average width of pore wall decreases with the increasing HF concentration from 1M to 4M.

The 1M01 SEM image is manifested in figure 3.9. During the first 10 minutes' anodization, the pores distribution is inhomogeneous. Prior to electrochemical anodization, the 4 inch silicon wafer was dipped into HF solution (10:1) for 10 seconds to remove the native SiO_2 on the surface. This process would create unevenly distributed pits on the surface due to the non-homogeneous nature of the native SiO_2, leading to the heterogenous distribution of the pores.

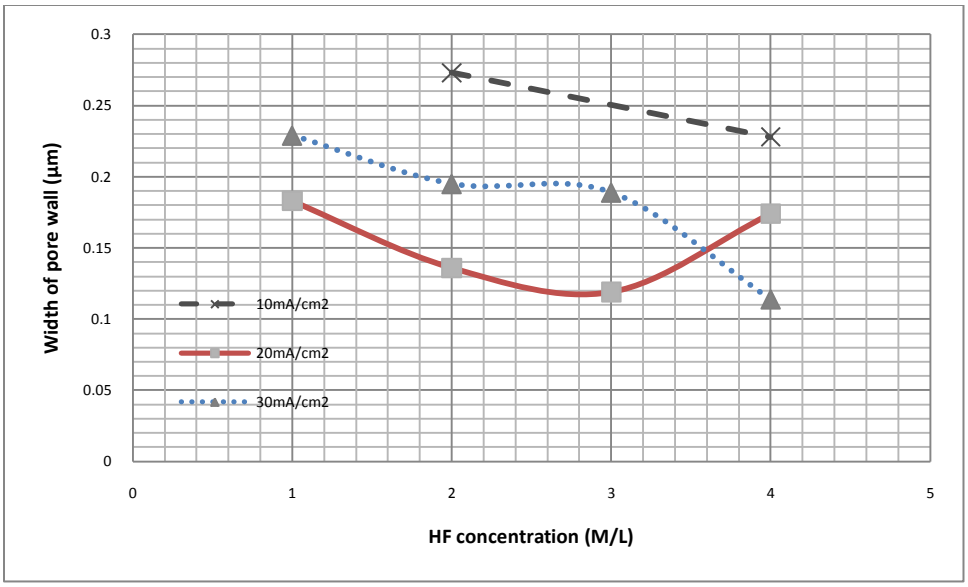

Figure 3.8 The variation of the width of the pores' wall with the different HF concentrations and current densities. The etching time is 20 minutes.

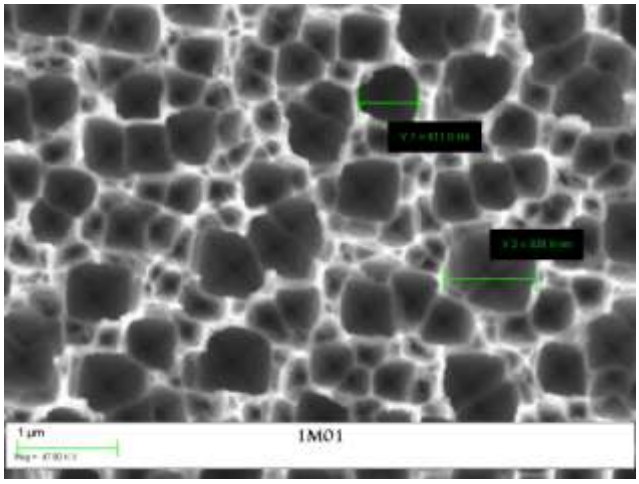

Figure 3.9 The top view SEM image of 1M01 sample.

The pore density N_p is defined as the number of pores per unit area. Observed from figure 3.10, the average pore density N_p are 0.482/µm^2, 0.656/µm^2, 0.519/µm^2 and 0.656/µm^2 at the 1M, 2M, 3M and 4M HF solution respectively, when the etching time is 20 minutes. By decreasing the current density to 20 mA/cm^2, the average pore density N_p

are 0.897/μm^2, 0.897/μm^2, 1.065/μm^2 and 0.346/μm^2 at the 1M, 2M, 3M and 4M HF solution respectively. From our experiments, the correlation among the pore density, current density and HF concentration is still ambiguous. With various HF concentrations and current densities, the average pore densities ranging from 0.35 to 1.07/μm^2.

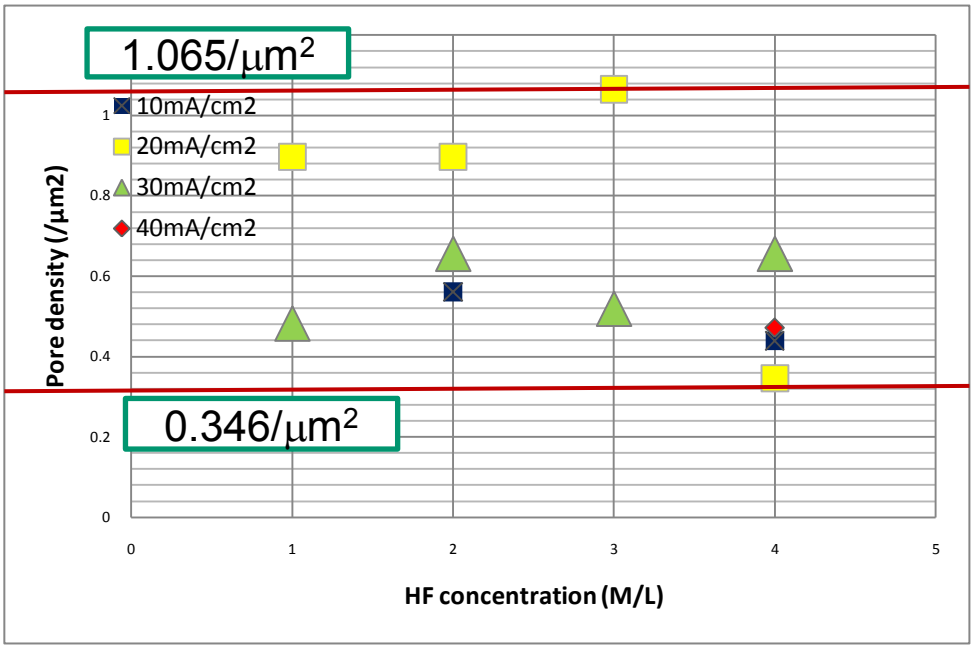

Figure 3.10 The variation of pore density N_p with the change of HF concentrations and current densities. The etching time is 20 minutes

On the one hand, the depth of macroporous silicon is achieved from cross-sectional SEM image. On the other hand, the variation of pore depth with adjustment of etching time and current density at 4M HF concentration is displayed in the figure 3.11, demonstrating a roughly linear increase with the etching time at a given current density. However, for a longer anodization etching time, chemical dissolution in the porous structure cannot be neglected which leads to a decrease in depth of the pore. For instance, the depths of pores are 89.4 μm for 55 minutes and 74.9 μm for 70 minutes.

In comparison with pore depth with different current densities (Table 3.4), the result shows that the pore depth is roughly proportional to the current density at a given anodization etching time.

Table 3.4 The variation of pore depth with the change of etching time and current density at 4M HF concentration (Unit: μm)

		Etching time (minutes)					
		10	20	30	40	55	70
current density (mA/cm^2)	10	3.8	15.6	35.7	N/A	N/A	N/A
	20	13.2	19.5	25.3	N/A	N/A	N/A
	30	6.3	41.4	46	N/A	N/A	N/A
	40	22.7	51.6	56.3	76.9	89.4	74.9
	50	N/A	N/A	46.5	N/A	N/A	106

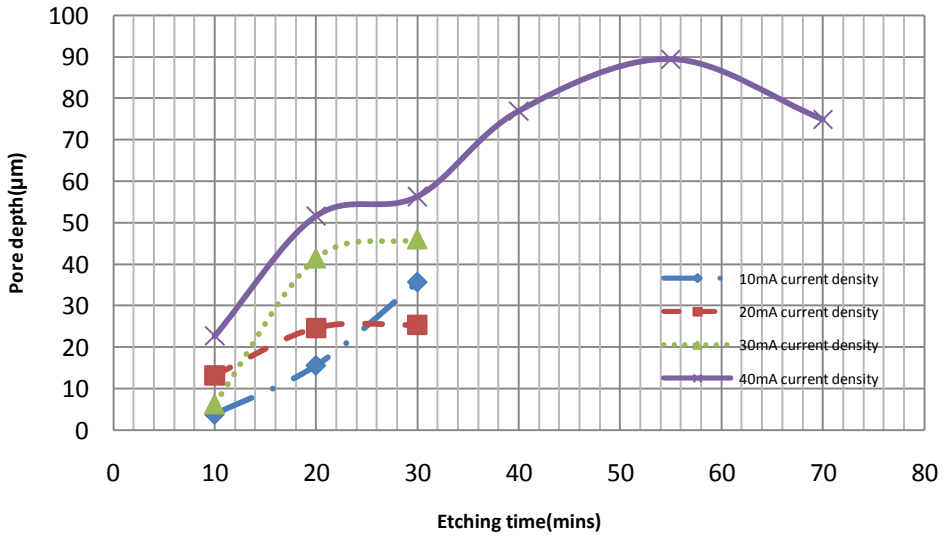

Figure 3.11 The variation of pore depth with the change of etching time and current density at 4M HF concentration

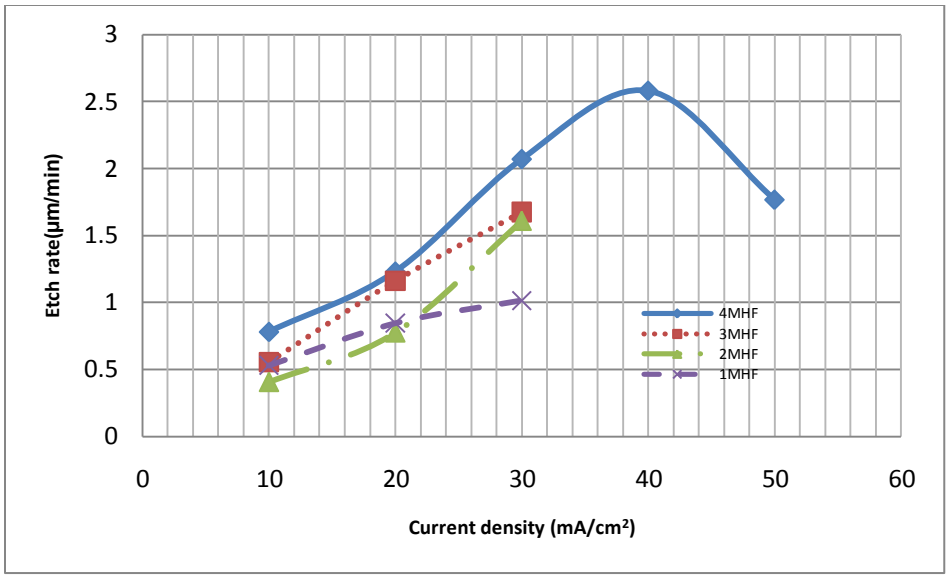

Figure 3.12 The variation of pore etch rate with different current densities and HF concentrations. The etching time is 20 minute.

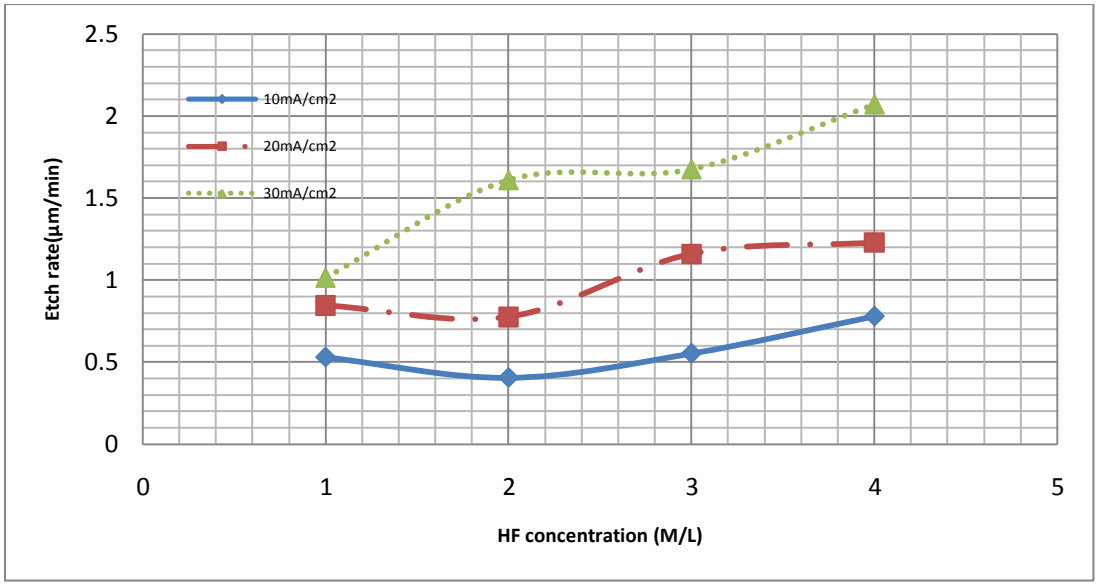

Figure 3.13 The variation of etch rate with the change of HF concentration. The etching time is 20 minute.

Figure 3.12 reveals how the etching rate of macroporous silicon depends upon the current density at different HF concentrations. It can be seen from the diagram that the

etch rate of a porous silicon at a given etching time increases with the current density from 10 mA/cm^2 to 40 mA/cm^2. At a large current density such as 50 mA/cm^2, the etch rate would become smaller than the ones at a lower current density due to the chemical dissolution in the porous structure.

Figure 3.13 disclosed how the etch rate of macroporous silicon relies upon the HF concentration at a variety of current density. The data shown in table 3.5 corresponds to the figure 3.13. It can be discerned from the diagram that the etch rate of porous silicon at a given etching time is unrelated with HF concentration.

Table 3.5 The variation of etching rate with different HF concentrations. The etching time is 20 minute. (Unit: μm/min)

		HF concentration (M/L)			
		10	20	30	40
current density (mA/cm^2)	10	0.53	0.41	0.55	0.78
	20	0.85	0.78	1.16	1.23
	30	1.02	1.61	1.68	2.07
	40	N/A	N/A	N/A	2.58

3.4 Summary

In this chapter, cylindrical macropore in the low doped p-type silicon substrate was fabricated using electrochemical etching in the solution of HF + DMF. The diameter, wall-width, and density of the PS were calculated by the OOF2 software. Table 3.6 shows the summarized characteristics of PS which includes diameter of pore, pore density, pore percentage, depth of pore and width of pore wall.

Table 3.6 The characteristics of porous silicon

Etching time (mins)	HF concentration (M/L)	current density (mA/cm^2)	Diameter (μm)	Pore density N_p ($/\mu m^2$)	pore percentage	Depth of pore (μm)	Width of pore wall (μm)
20	1	**20**	0.873	0.897	53.7%	16.9	0.183
		30	1.214	0.482	55.6%	20.3	0.229
	2	**10**	1.061	0.561	50.3%	8.1	0.273
		20	0.919	0.897	59.5%	15.5	0.136
		30	1.043	0.656	56.4%	32.2	0.195
	3	**20**	0.850	1.065	60.5%	23.2	0.119
		30	1.197	0.519	59.4%	33.5	0.189
	4	**10**	1.282	0.439	62.6%	15.6	0.228
		20	1.526	0.346	63.3%	24.6	0.174
		30	1.121	0.656	64.2%	41.4	0.114
		40	1.378	0.472	70.3%	51.6	0.078
30		**40**	0.832	1.292	70.2%	56.3	0.048

It is evident that the flexibility of pore design is poor under the condition of low doped p-type Si (1-20 Ω cm) and the solution of HF + DMF. But some useful conclusions can be withdrawn as below:

1) The **average** diameters of the pores are in the range between 0.85μm to 1.53μm.

2) The pore depth increase roughly linearly with the etching time at a given current density.

3) The etch rate of porous silicon at a given etching time increases with the current density.

Chapter 4 Electrochemical Characteristics of Porous Si as Anode for Li-ion Batteries

4.1 Assembling lithium ion cell for testing

In this work, the electrochemical performances of PS as anode were examined versus Li in a Swagelok-type half-cell which consists of a bottom cap, a Teflon cylinder, a spacer, and a closing cap (figure 4.1).

(a) (b)

Figure 4.1 (a) Swagelock Cell, (b) Various parts in the assembly of swagelock cell.

At first, to assemble the cell, after being dried in vacuum oven at temperature 120˚C for 12 hour, the PS specimen was laid into the bottom cap as working electrode. No binders or conducting carbon were employed. Secondly, a separator was placed on top of the PS anode. The battery separator was trilayer PP/PE/PP electrolytic microporous membrane provided by Celgard (Figure 4.2). The separator worked as a barrier between the anode and the cathode while enabling the exchange of lithium ions from one side of the battery to the other. The separator was carved into a circle and dried

in vacuum oven at temperature 120˚C for 12 hours. Thirdly, the Teflon cylinder was inserted tightly onto the bottom cap. Fourthly, Li foil purchased from Aldrich, which works as both reference and counter electrodes, was placed inside the cylinder on the top of separators. Last but not least, the liquid electrolyte, which is 1 M $LiPF_6$ in a 1:1 mixture of ethylene carbonate and dimethyl carbonate, is dropped into the cylinder and the cell is tightly packed using spacer with screw cap.

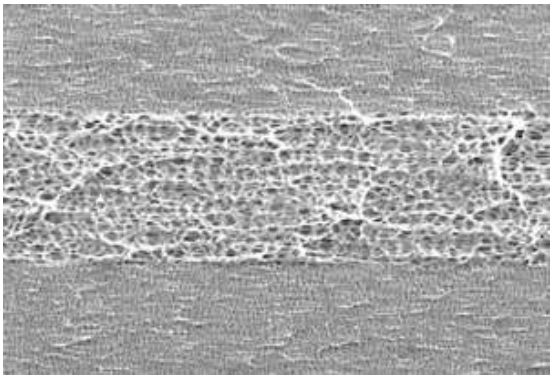

Figure 4.2 SEM Cross-Section Photomicrograph of Celgard® Trilayer PP/PE/PP Battery Separator[62]

Figure 4.3 Picture of Glove Box.

The glove box used to assemble the Swagelock cell (Figure 4.3) is manufactured by *Vacuum Atmospheres Company*. The glove box controls the atmosphere under argon with an oxygen and moisture level below 0.5 ppm at 1 atm pressure and room temperature.

4.2 Galvanostatic testing approach of Lithium intercalation in PS

4.2.1 Galvanostatic discharge/charge test

A computer-controlled Land CT2001A electrochemical working station (**Figure 4.4**) was made to control the constant current to charge/discharge the cell, recorded its potential as a function of time and tested the capacity of the PS anode at ambient conditions The cells were galvanostatically charged and discharged at a current density of 50μA within the range of 0.01–3.0 V versus Li, i.e. discharging was stopped when the electrode potential approached 0.01 V vs. Li/Li^+ (end-of-discharge potential) and charging was stopped when the electrode potential approached 3V vs. Li/Li^+ (end-of-charge potential). For the half-cell, the discharge capacity is the total charge inserted into the porous Si per mass unit, during Li insertion, whereas the charge capacity is the total charge removed during Li extraction. All Swagelok-type half-cells were assembled in a glove box and tested at ambient condition.

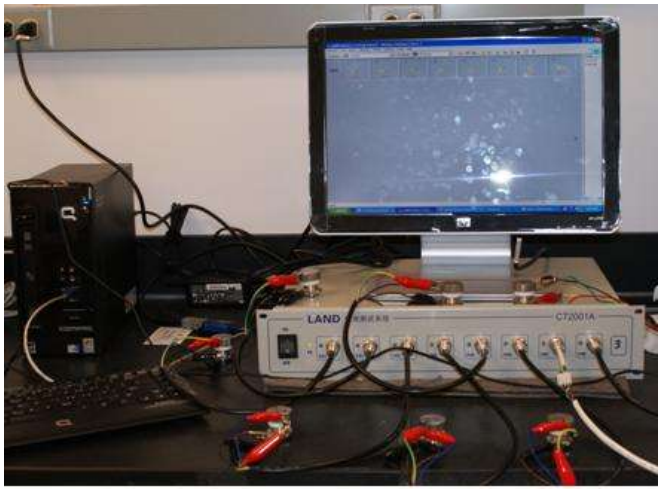

Figure 4.4 Battery Testing Station (Land CT2001A)

4.2.2 Cyclic voltammetry test

Figure 4.5 Gamry Potentiostat

Gamry Potentiostat (Figure 4.5) is conducted to conduct cyclic voltammetry (CV) analysis for the mechanistic study of redox systems. Cyclic voltammetry enables the electrode potential to be rapidly scanned in search of redox couples, the current at the working electrode is measured during the specific potential scan rate, such as 50mV/s, 20mV/s and 0.2mV/s between open circuit potential (OCP) and 2V or 3V versus Li for

the back and forth sweeps. The resulting current-potential curve is called cyclic voltammogram.

The electrochemical performance of the non-free-standing porous Si (PS) as anode of LIBs was investigated by cyclic voltammetry test. The PS anodes are prepared by different anodization etching time, such as 10, 25, 40, 55, 70 minutes respectively (table 4.1), under the condition of the 4 M HF concentration and 40 mA/cm^2 current density. The PS is not separated with the silicon substrate and coated on the backside of samples with Cu, Au and Pt by electron beam evaporator respectively.

Table 4.1 The various non-free-standing PS prepared for the anode of LIBs

No.	**Thickness (μm)**	**Etching time (mins)**
1	22.7	10
2	54	25
3	76.9	40
4	89.4	55
5	74.9	70

4.3 Results and discussion

In this work, the open circuit potential of the Lithium ion cell with porous Si as anode is about 3.0V vs. Li/Li^+ in the open-circuit state, which is approximately equal to the theoretical value vs. Li/Li^+ in the open-circuit state.

In general, when Li^+ moving under the electric force, there are several basic steps pertinent: Li ions accumulating on the surface of electrode, incorporating into the electrode lattice structure, and diffusing away from the electrode surface.

4.3.1 Fast scan rate of CV

From the figures 4.6-4.9, the reduction current density peaks (absolute value) of PS are greater than the ones of flat silicon film. At the 50mV/sec of the scan rate, the reduction current density peak during the first cycle is -3.21 mA/cm^2 for the sample with the deepest depth of pore at the 55minutes of etching time. Since no redox pair peaks were observed in the forward and backward curves under the fast scan rate (50mV/s), it is possible that Li ions accumulation on the electrode are dominant. The peaks are related with the double layer capacitance, which correlated with the electrode surface area. When the scan rate is reduced to 20mV/s, a weak oxidation peak was observed in the specimens with deep pores. The appearance of the weak oxidation peak suggested that a small amount of Li has been inserted into the Si structure and now removed from the Si.

From the table 4.2 which corresponds to the figure 4.6-4.9, the reduction current density peaks (absolute value) increase roughly with the depth of porous silicon. This indicated that the depth of the pore which can provide more surface area would affect the surface accumulation and lithiation process. However, the peak current density by deep pore was just slightly higher than the one by shallow pore. This accounts for that only a small portion of the deep pores took part in the electrochemical process. The reduction current density peaks (absolute value) increase with scan rate from low 20mV/sec to 50mV/sec. The electrochemical reaction may be affected by surface reaction and diffusion of Li^+ [63]. Under the condition of surface reaction, the peak current is proportional to scan rate. For the diffusion of Li^+, the peak current is proportional to the square root of scan rate. The reduction current density peaks (absolute value) decrease with the progressive cycle number at a specific scan rate, such as 50mV/sec or 20mV/s. It

is conceivable that the high cycling rate blocks further accumulation and lithiation through the complete depth of the PS or the flat silicon film.

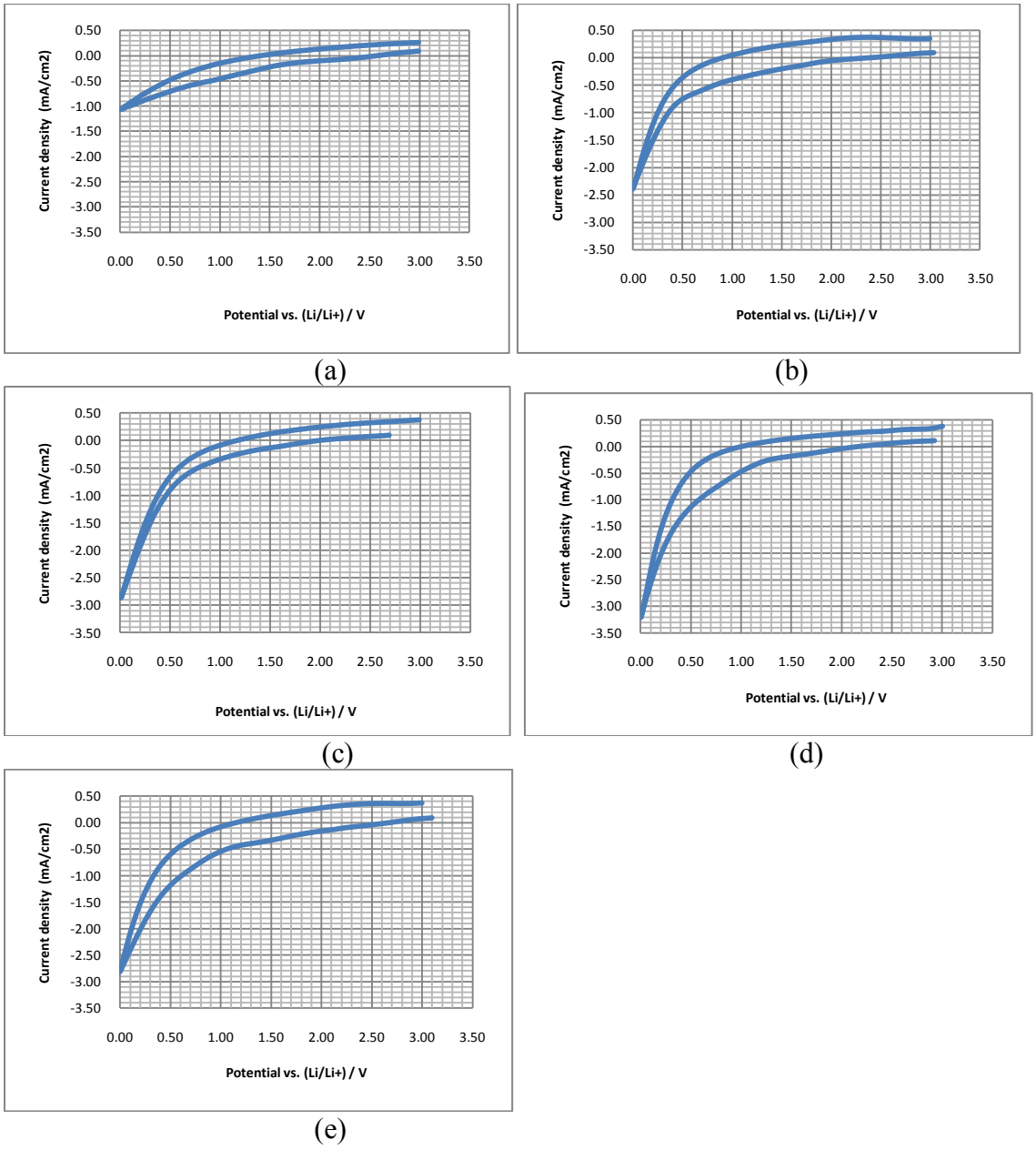

Figure 4.6 The first cycle of cyclic voltammogram for PS as anode in LIBs. Scan rate: 50mV/s, backside metal: Gold (a) Silicon (b) PS at 10 mins of anodization etching (c) PS at 40 mins of anodization etching (d) PS at 55 mins of anodization etching (e) PS at 70 mins of anodization etching

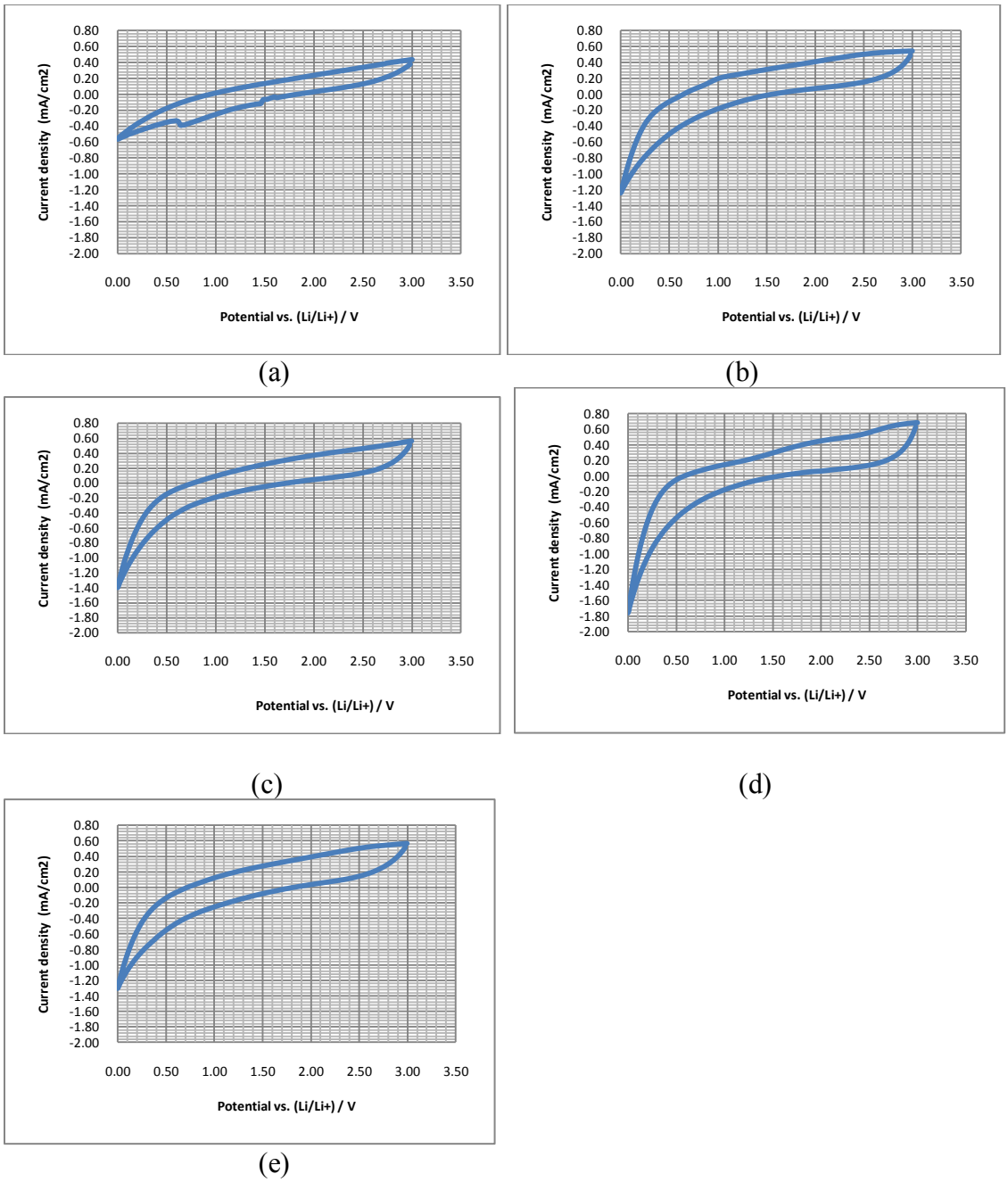

Figure 4.7. The fifth cycle of cyclic voltammogram for PS as anode in LIBs. Scan rate: 50mV/s, backside metal: Gold (a) Silicon (b) PS at 10 mins of anodization etching (c) PS at 40 mins of anodization etching (d) PS at 55 mins of anodization etching (e) PS at 70 mins of anodization etching

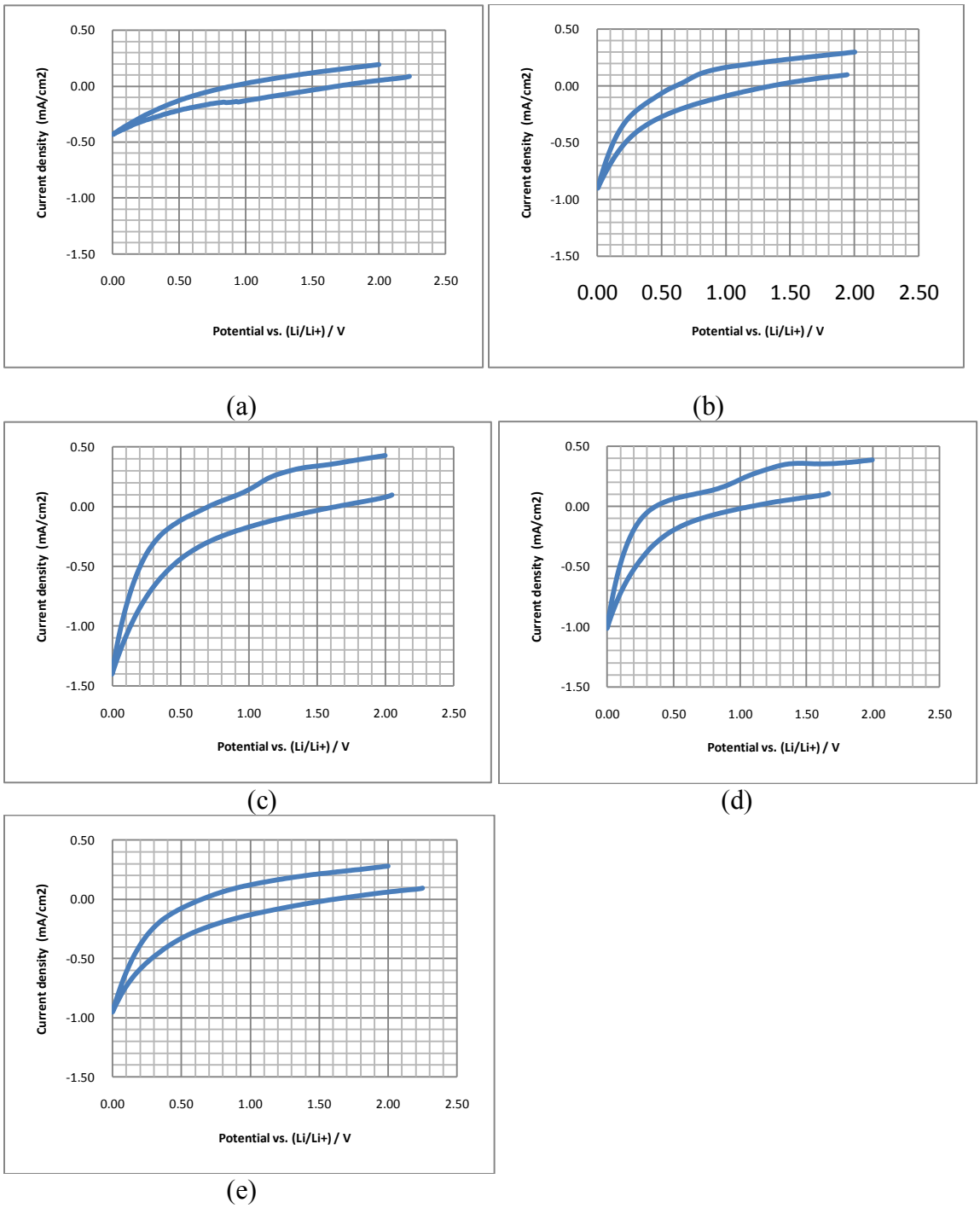

Figure 4.8 The first cycle of cyclic voltammogram for PS as anode in LIBs. Scan rate: 20mV/s, backside metal: Gold (a) Silicon (b) PS at 10 mins of anodization etching (c) PS at 40 mins of anodization etching (d) PS at 55 mins of anodization etching (e) PS at 70 mins of anodization etching

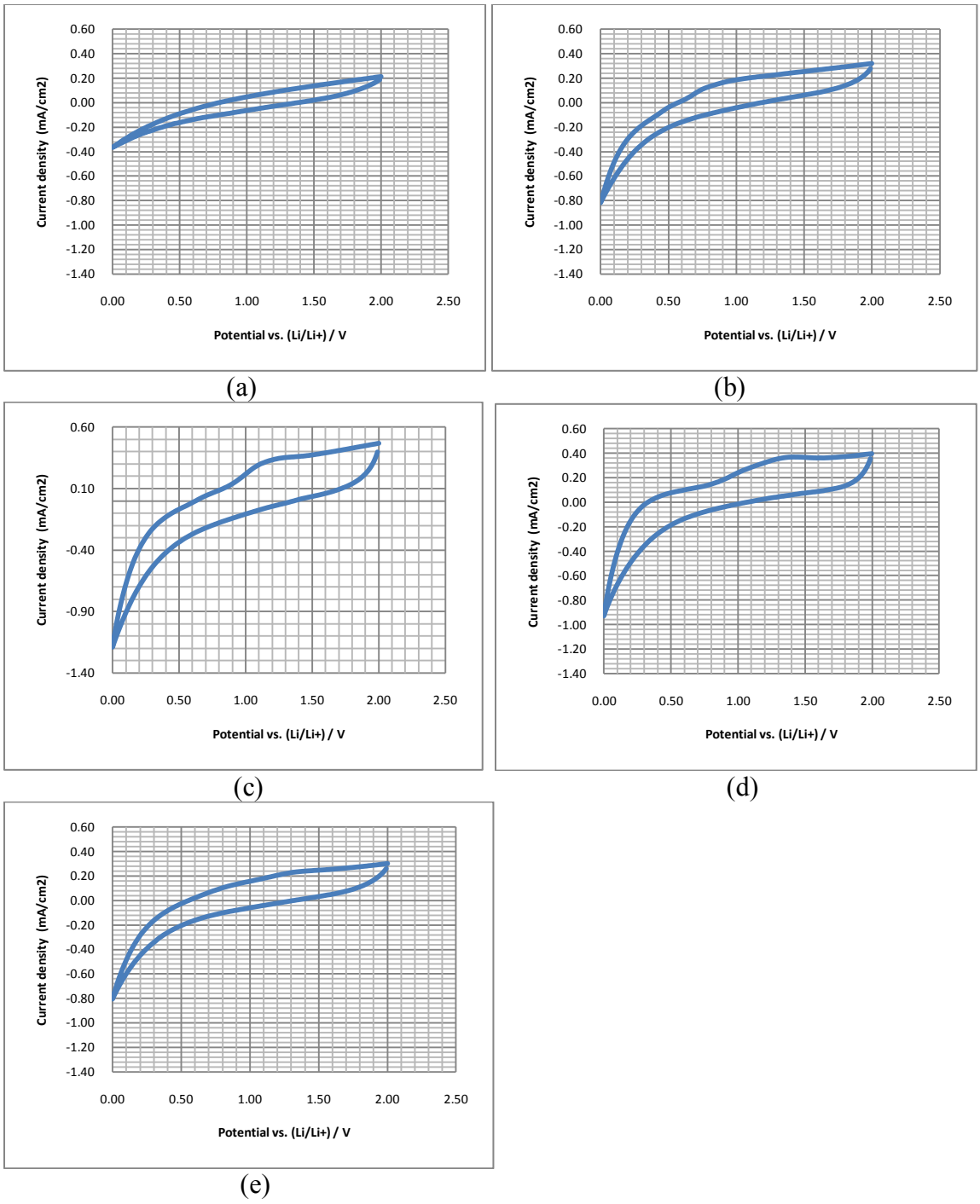

Figure 4.9 The second cycle of cyclic voltammogram for PS as anode in LIBs. Scan rate: 20mV/s, backside metal: Gold (a) Silicon (b) PS at 10 mins of anodization etching (c) PS at 40 mins of anodization etching (d) PS at 55 mins of anodization etching (e) PS at 70 mins of anodization etching

Table 4.2 Comparison of the reduction current density peaks at the different scan rate

	Reduction current density at 1st cycle, rate 50mV/s (mA/cm^2)	Reduction current density at 5th cycle, rate 50mV/s (mA/cm^2)	Reduction current density at 1st cycle, rate 20mV/s (mA/cm^2)	Reduction current density at 2nd cycle, rate 20mV/s (mA/cm^2)	Depth of the microtube (μm)
Si	-1.06	-0.56	-0.43	-0.36	0
PS 10mins	-2.39	-1.24	-0.90	-0.82	22.7
PS 40mins	-2.87	-1.39	-1.04	-0.92	76.9
PS 55mins	-3.21	-1.76	-1.01	-0.93	89.4
PS 70mins	-2.81	-1.30	-0.95	-0.80	74.9

4.3.2 Slow scan rate

4.3.2.1 Comparison of PS and flat silicon as anode

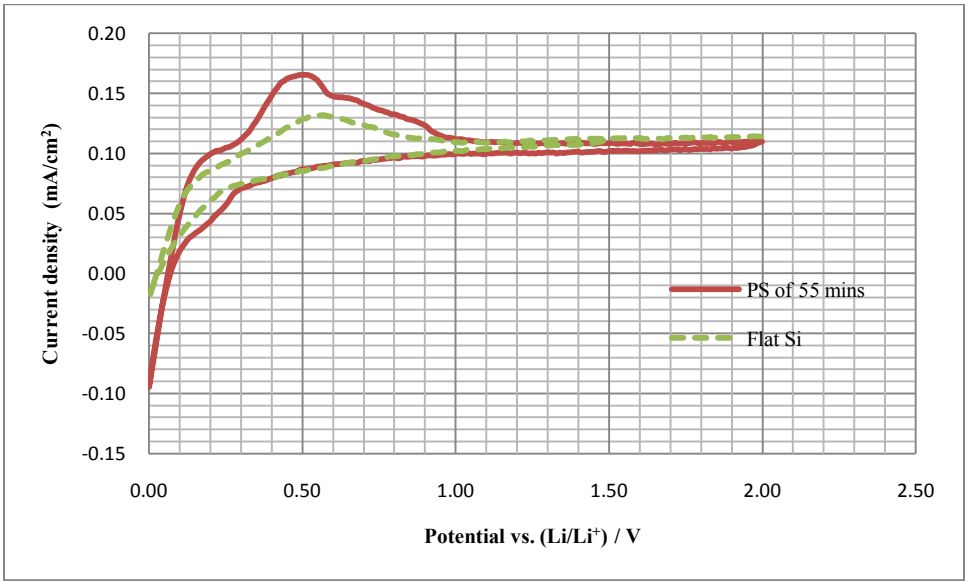

Figure 4.10 Comparison of the cyclic voltammograms of PS and flat silicon as anode in LIBs.

Fig. 4.10 compares the cyclic voltammograms of PS and flat silicon as anode in LIBs at 0.20mV/s of scan rate. The area difference between the reduction peak and the

oxidation peak of the PS anode is much smaller than that of the flat Si anode, which indicates that the PS anode denotes better reversibility than flat Si. This might be due to the fact that lithium ions and PS have larger contact area than pure flat silicon, which facilitates the lithium insertion/removal process and thus compensate for the capacity loss.

From the table 4.3 which corresponds to the figure 4.10, the reduction current density peak for PS is -0.09 mA/cm^2 which is about five times greater than the maximum value of reduction current density peak for flat Si (-0.02 mA/cm^2), this explicitly explain that the specific capacity of PS is higher than the one of flat Si due to the enlarged surface area of PS. The sharp oxidation peak of flat Si (0.107 mA/cm^2) is smaller than the sharp oxidation peak of PS (0.166 mA/cm^2), which indicates that the amount of active materials of PS for the delithiation is more than flat Si due to the enlarged surface area of PS.

Table 4.3 comparison of the cyclic voltammograms between PS and flat silicon as anode in LIBs

	Reduction current density peak at 2nd cycle, rate 0.20mV/s (mA/cm^2)	Oxidation current density peak at 2nd cycle, rate 0.20mV/s (mA/cm^2)	Voltage range Corresponds to oxidation Current density peak (V)	Voltage range Corresponds to reduction Current density peak (V)	Depth of PS (μm)
Si	-0.02	0.107	0.5-0.6	0.01	0
PS 55mins	-0.09	0.166	0.5	0-0.2	89.4

4.3.2.2 Cyclability and stability

Figure 4.11 (a) is the cyclic voltammogram of the PS fabricated by 55 minutes of anodization etching. The reduction current density peaks (absolute value) are -0.06 mA/cm^2, -0.20 mA/cm^2 and -0.34 mA/cm^2 at the first cycle, fifth cycle and 10th cycle

respectively, which explicates the formation of Li-Si phases enhances with the progressive cycle numbers.

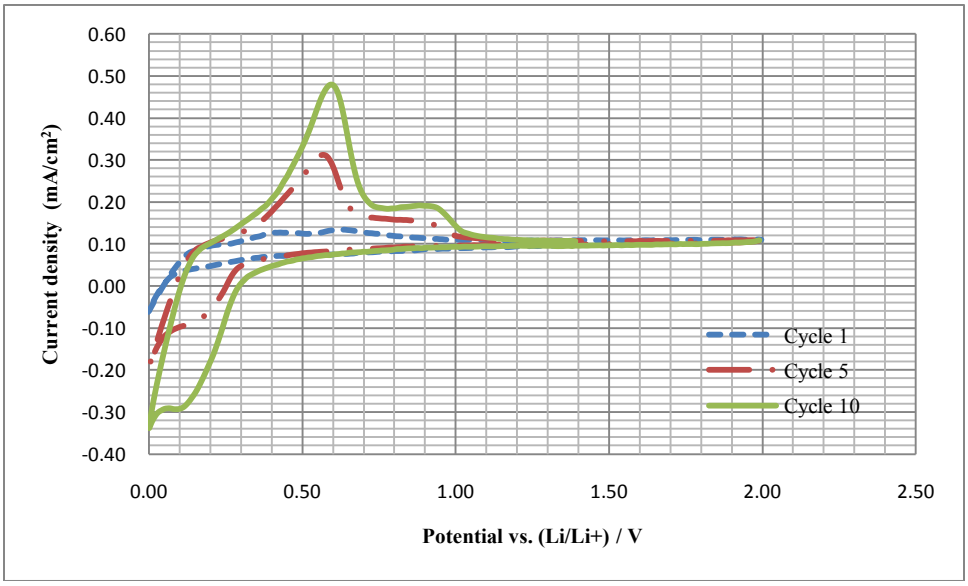

(a)

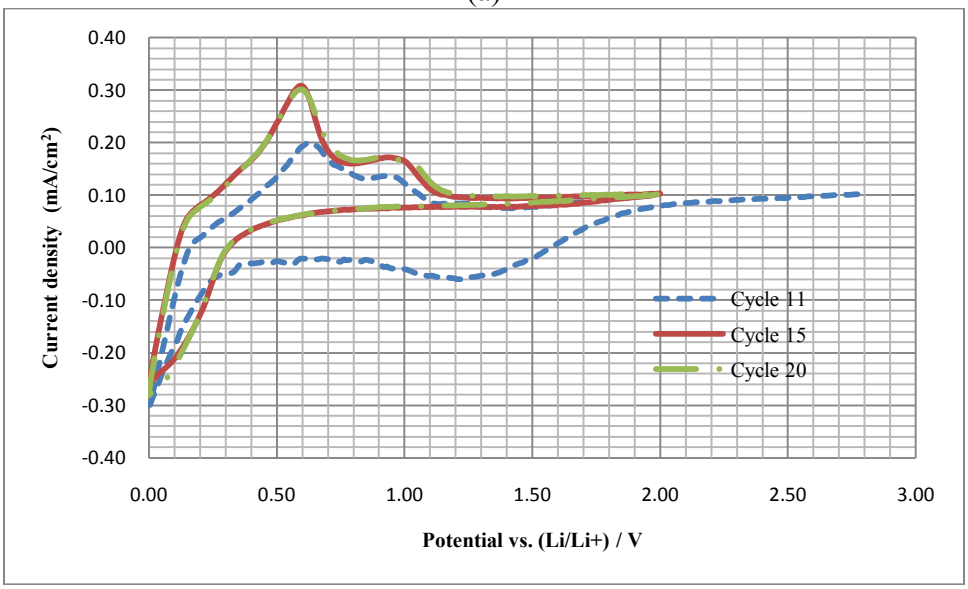

(b)

Figure 4.11 Cyclic voltammogram of PS as anode in LIBs. Scan rate: 0.2mV/sec in the potential range 0-2V. The PS was fabricated under the condition of 55 minutes of anodization etching time, 4 M HF concentration and 40 mA/cm^2 current density. (a) cycle 1 to cycle 10. (b) cycle 11 to cycle 20 was tested with the same cell 6 days later.

The sharp oxidation peak current density gained with cycling up to the 10th cycle, which indicated that the electrode was activated and the charge transferred during the redox reactions.

The eleventh cycle was performed with the same cell 6 days later (figure 4.11 (b)). The sharp oxidation current density peak decreases from 0.48 mA/cm^2 at the 10th cycle to 0.20 mA/cm^2 at the 11th cycle, which results from the diffusion of Lithium ions at the surface of sample. In addition, it is noted that the current of the reduction peak slightly reduces with cycling from -0.30 mA/cm^2 at the 11th cycle to -0.27 mA/cm^2 at 20th cycle. Meanwhile, the oxidation peak current density was aggrandized with cycling from the 0.20 mA/cm^2 at the 11th cycle to the 0.30 mA/cm^2 at 20th cycle, none of them can obtain the oxidation peak current density 0.48 mA/cm^2 at the 10th cycle, which indicated there was a capacity degradation that was attributed to an increased polarization that hindered electrochemical interface kinetics in the cell. The first reduction current peaks originate from the formation of SEI films due to decomposition of electrolyte on the film surface at the cycle 11 in figure 4.11 (b), which disappear from the subsequent cycles.

The discharge and charge curve is stable from the cycle 15 to cycle 20 in figure 4.11 (b), which indicates that lithium diffusion and electrochemical kinetics reach an optimal state. The PS as anode shows a good cyclability and stability.

4.3.3 SEM images of slow scan

The observed activation phenomenon is ascribed to the reconstruction of crystal structure at the wall surface of porous Si (SEM images shown in **Figure 4.12**). The deviation is shown in **Figure 4.12**(b) to (e), the main cause for the fade in capacity.

There is a remarkable contrast in the changes of wall surface morphology between the SEM images before Li insertation/extraction process (**Figure 4.12**(a)) and the ones after Li insertation/extraction process (**Figure 4.12**(b)-(e)).It is visible that the surface of the PS wall prior to working as anode of LIBs is smoother than those surface of the PS wall after Li insertation/extraction process. The surface of pore wall has a turnover, and shows agglomerates of Si particles found on the surface of pore wall due to the large volume expansion during Li insertation/extraction process, which affects the electrochemical kinetics and the diffusion of the lithium ions on the surface of the PS wall. It is evident that these agglomerates of Si particles provide more surface area for lithiation process. Therefore, higher lithium incorporation could become possible in subsequent cycles due to the agglomerates of formation in the pore wall surface, which results in the reduction current density peaks (absolute value) increasing with the progressive cycle from cycle 1 to cycle 10 (**Figure 4.11**(a)). After a longer time, the lithium ions to completely alloy with silicon, which results in the reduction current density peaks are stable at -0.30mA/cm^2 (**Figure 4.11**(b)).

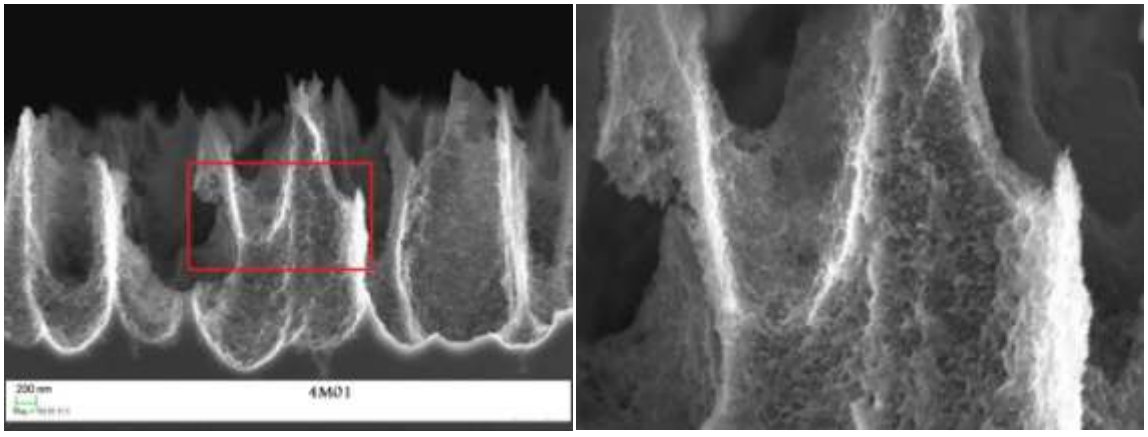

(a)

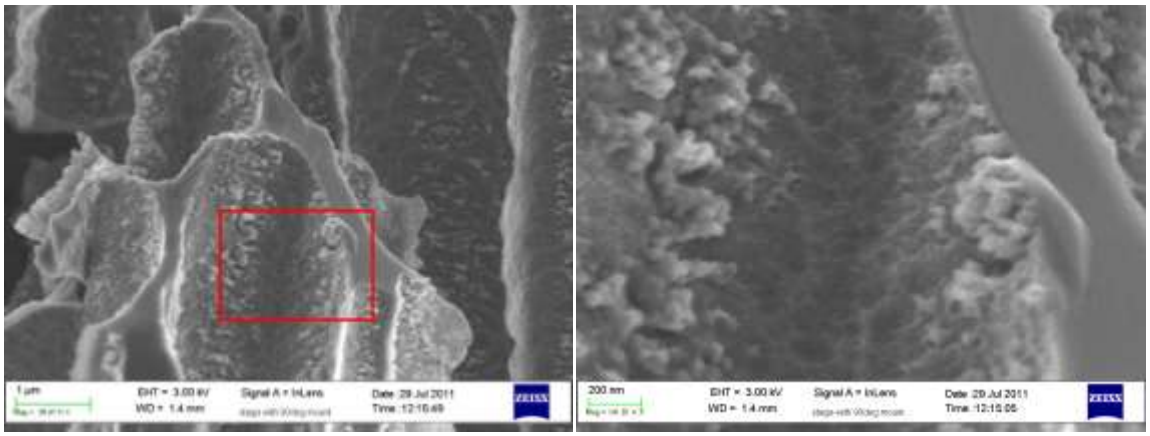

(b)

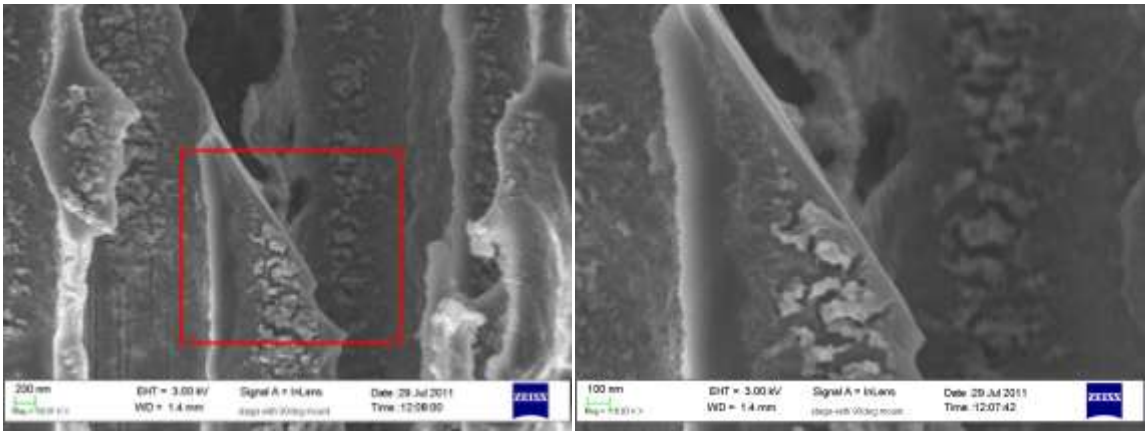

(c)

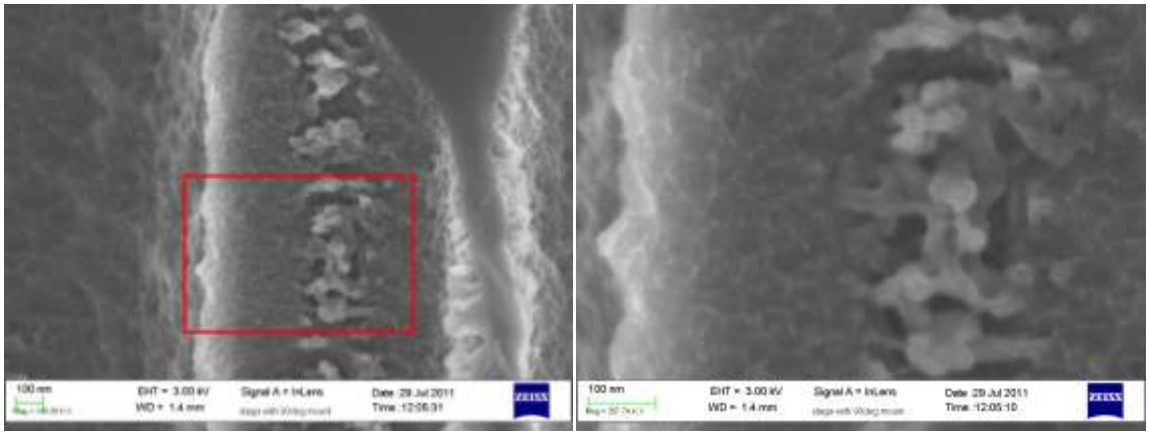

(d)

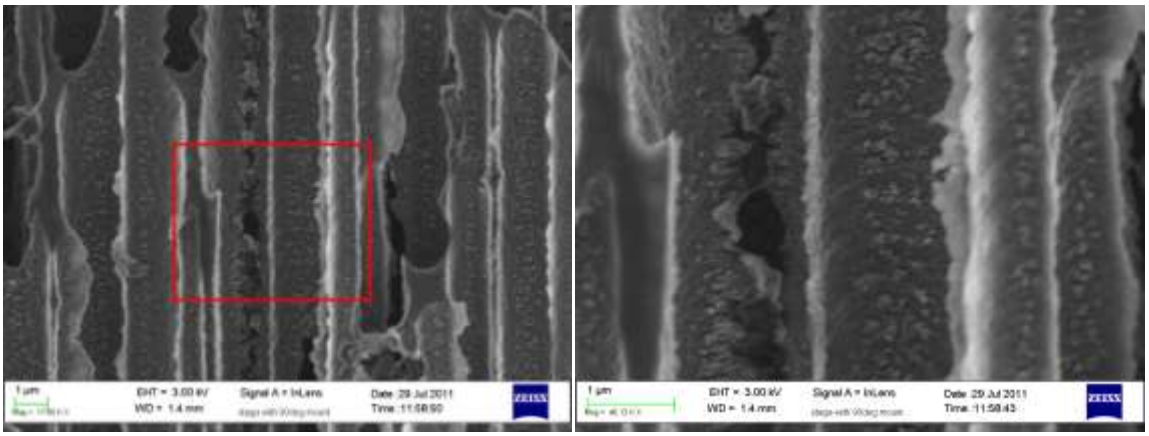

(e)

Figure 4.12 The SEM images of change of the PS wall with a magnified image of each sample. (a) the microtube wall without Li insertation/extraction process (b)-(e) the change of the PS wall after Li insertation/extraction process.

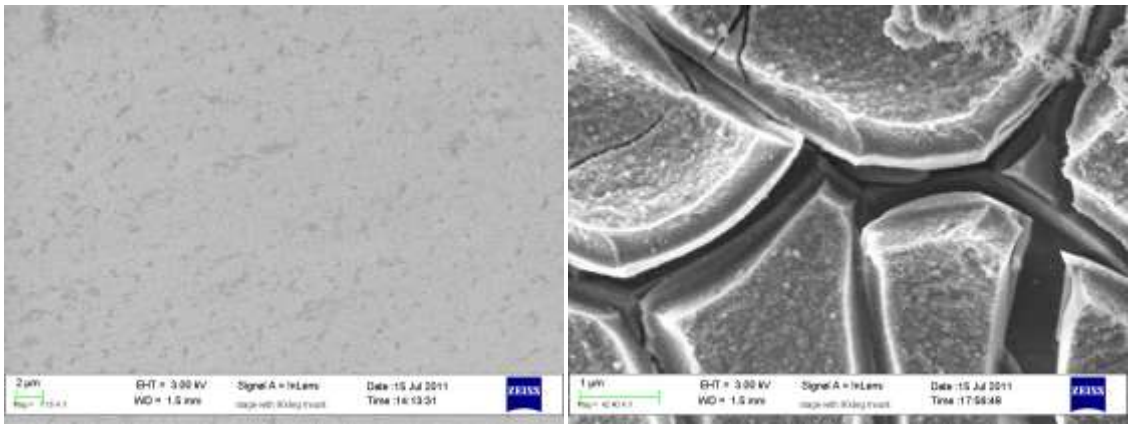

(a) (b)

Figure 4.13 The images of SEM for the pure flat silicon film as anodes of LIBS, (a) before CV cycling, (b) after test for 10 cycles.

As for those samples of flat Si, the surface of silicon partially cracked after CV testing for 10 cycles (**Figure 4.13** a and b). This morphology mutation is mainly because of the significant internal tension leading to the large volume expansion/contraction in the Lithium ion insertion/extraction process [63], which can interfere considerably the

effective transportation of electrons, and hence deteriorate the anodic performance. These results are in good agreement with the quick fade in capacity.

4.3.4 Estimation of Li insertion capacity

In order to figure out the mass of the PS exclusive of the connected silicon substrate, the parameters which include the area percentage of pore and the depth of pore should be obvious.

In this work, the depth can be measured from the image of SEM. The area percentage of pore should be calculated by the OOF2 mentioned from the above chapter for finite element analysis of microstructure, the macroscopic properties can be received by the images of real or simulated microstructures. The Ubuntu Linux system was employed for the running of OOF2. Uploading the top view of SEM image, the area of pore can be distinguished by the color at the 0.076 of delta_gray parameter. The red color region is the area of pore shown in the figure 4.14.

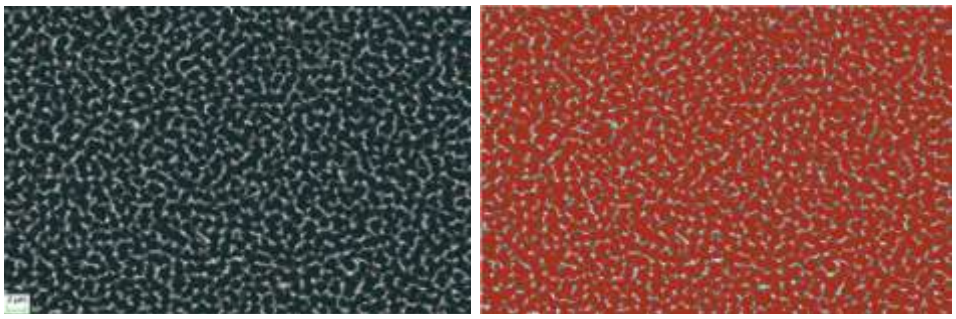

(a) (b)

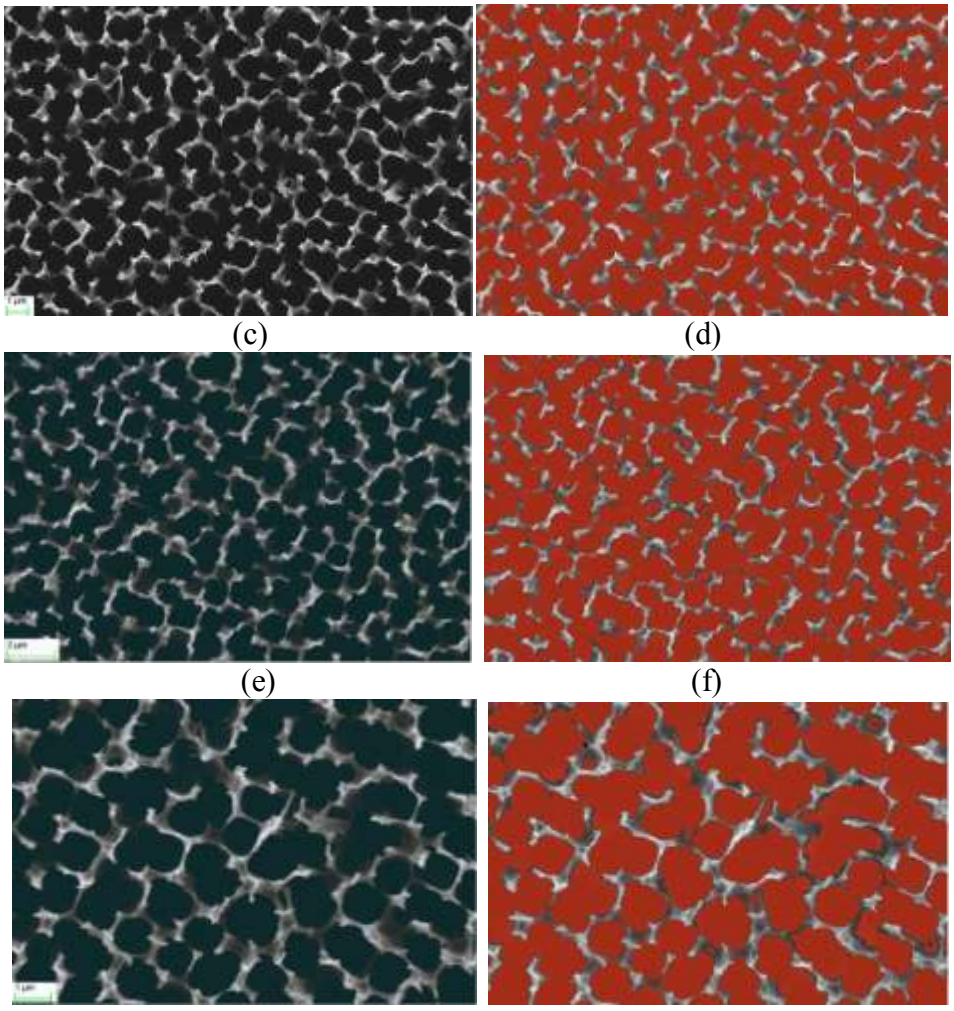

(c) (d)

(e) (f)

(g) (h)

Figure 4.14 Calculation of area percentage of pore by OOF2, (a) (c)Top view of SEM image (4M HF, 40 mA/cm^2 and 20 minutes of etching time), (b) (d) the SEM image of (a) (c) calculated by OOF2 respectively, (e) (g) Top view of SEM image (4M HF, 40 mA/cm^2, 30 minutes of etching time), (f) (h)the SEM image of (e)(g) calculated by OOF2 respectively.

There are two classes of PS which were fabricated by different etching time and the same current density and HF concentration. Figure 4.11 (a) and (c) show different part of the PS fabricated by 4M HF, 40 mA/cm^2 of current density and 20 minutes of etching time. Figure 4.11 (e) and (g) show different part of the PS fabricated by 4M HF, 40 mA/cm^2 of current density and 20 minutes of etching time.

The area of figure 4.11(a) is 1024× 670 pixels, the red color region shown in figure 4.11(b) is 499004 pixels, the area percentage of pore for the figure 4.11 (a) is

72.7%. The area of figure 4.11(c) is 1024× 672 pixels, the red color region shown in figure 4.11(d) is 500243 pixels, the area percentage of pore for the figure 4.11(c) is 72.7%. The area of figure 4.11(e) is 1019× 671 pixels, the red color region shown in figure 4.11(f) is 499656 pixels, the area percentage of pore for the figure 4.11(e) is 73.1%. The area of figure 4.11(g) is 1022× 675 pixels, the red color region shown in figure 4.11(h) is 495232 pixels, the area percentage of pore for the figure 4.11(g) is 71.8%.

At last, the average area percentage of pore at 4M HF and 40 mA/cm^2 of current density is 72.5%.

So the 27.5 % of the volume of the sample is PS wall structure.

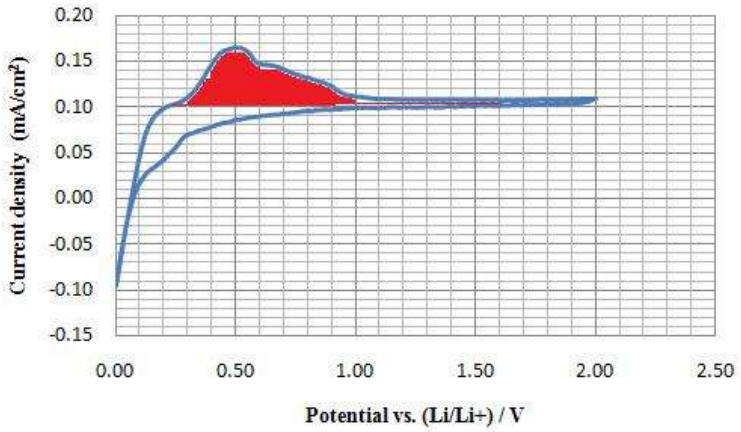

Figure 4.15 The second cycle of cyclic voltammogram for PS at 55 mins of anodization etching as anode in LIBs. Rate: 0.20mV/s, backside metal: Gold.

The total quantity of charge at the second cycle of the PS as anode is 0.885 coulomb which can be read from integrated calculation of CV with the red color region in figure 4.15. Because 1 mAh is equal to 3.6 C, the 0.885C should be 0.246mAh. So the mass of the sample is,

The mass of the sample =Volume of the sample × silicon density × 27.5%

The depth of pore is 89.4μm, the area of the sample is 0.9cm^2, so the mass of the sample is 5.15 mg.

The capacity of this sample at the second cycle of the PS of 55 minutes is 47.7 mAh/g. The small value of capacity of the PS results from the uncompleted lithiation of the PS active material due to quick scan rate of CV test. As can be seen from SEM images (4.12b) , only a small portion (less than 10 percent in thickness) of the Si walls participated in the lithiation/delithiation process at the 0.2mV/s scan rate. When this incomplete factors were accounted for, the actual Li storage capacity can reach over 500mAh/g. Quantitative determination of the Li storage capacity in the porous Si supported on Si wafer is one of the suggested future research.

4.3.5 Galvonostatic discharge and charge

To accurately examine the capacity and voltage plateau of the free-standing PS thin film peeled off from the silicon substrate, a low current discharge/charge test was carried out at the rate of 50μA. **Figure 4.16** shows the first and second discharge/charge curves of the PS as anode between 0 and 3 V versus Li/Li$^+$. The PS film is dried in the vacuum oven and not coated by metal. The first discharge capacity of the PS is 1425 mAh/g. The first charge capacity (reversible capacity) of the PS is 1150mAh/g, which is much higher than that of a graphite anode (320 mAh/g). The second charge capacity (reversible capacity) of the PS is 1035mAh/g. In the first discharge stage relevant to the Li-insertion into the PS(**Figure 4.16**), the appearance of the sloping potential plateau represents for the formation of SEI film in connection with the electrolyte decomposition,

while the lithiation and delithiation take place in a voltage range of 0.1–0.01V and 0.1–1.2V vs. Li/Li^+ respectively.

The plateau of the first discharge curve (**Figure 4.16**) was mounted up to 0.1V after reaching the 0 V, this indicates that the over potential is lessened since the resistivity of interface between the electrolyte and PS was receded.

The irreversible capacity may result from the formation of a SEI layer in the first cycle. The growth of a solid–electrolyte interface (SEI) film begins between 1 V and 0 V at the first discharge process and disappears in the second cycle.

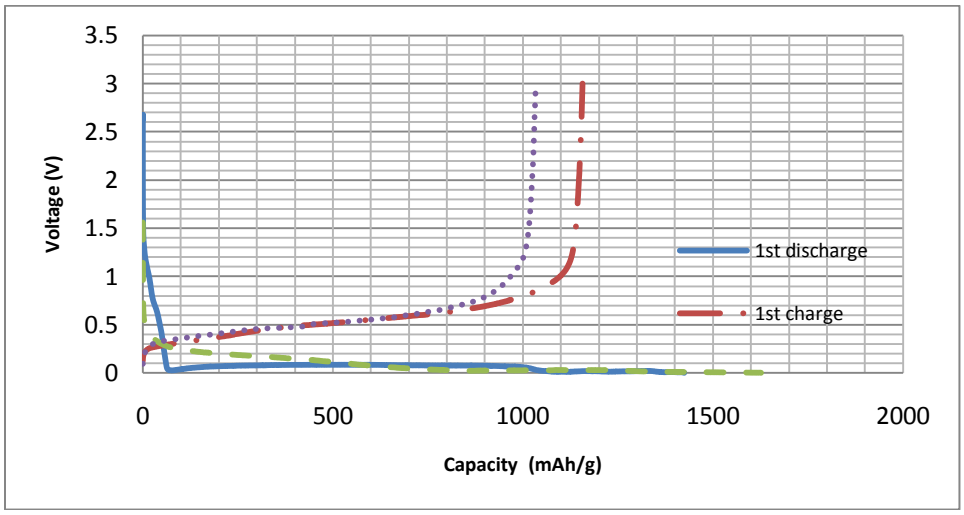

Figure 4.16 Discharge/charge curves of PS thin film as anode of LIBs at the rate of 50μA

After 2 cycles, the retention of capacity faded quickly, the possible degradation mechanisms are as below. (1) Mechanical disintegration of the Si occurs during a significant volume change. (2) The irreversible loss of capture ability of lithium ions caused by a significant number of insertion-generated defects inside the Si lattice, which is due to the reacted anode material, was no longer available for electrochemical reaction [37]. (3) The phase transition from crystalline into amorphous state after the first cycle

also induces some irreversible capacity. (4) The assembly of the cell would affect the performance of LIBs, when the cap of cell was screwed up loosely, the capacity of the test should be lower than the ones which were tightly screwed up.

4.3.6 Cyclic voltammograms with coated copper on the backside of sample

From the table 4.4, the reduction current density peaks (absolute value) of PS are generally larger than the ones of flat silicon film and enlarge roughly with the etching time of PS.

Table 4.4 Comparison of the cyclic voltammograms at the various depths of PS as anode in LIBs(Copper)

	Reduction current density peak at 1st cycle, rate 50mV/s (mA/cm^2)	Reduction current density peak at 5th cycle, rate 50mV/s (mA/cm^2)	Reduction current density peak at 1st cycle, rate 20mV/s (mA/cm^2)	Reduction current density peak at 2nd cycle, rate 20mV/s (mA/cm^2)
Si	-7.40	-2.93	-2.13	-1.78
PS 10mins	-12.29	-5.09	-3.61	-2.86
PS 25mins	-18.07	-5.92	-3.88	-3.32
PS 40mins	-13.91	-6.87	-5.22	-3.99
PS 55mins	-7.16	-3.76	-2.89	-2.41
PS 70mins	-3.33	-1.59	-1.00	-0.83

This reproved that the depth of the pore is useful for the lithiation process. The test sample with copper on the backside showed the similar characteristics as the sample with gold on the backside mentioned in the section 4.3.1. The part of the deep pore plays an important role in the lithiation and delithaition process due to the peak of current

density increasing with the pore depth. The high cycling rate blocked full lithiation through the complete depth of the PS or the flat silicon film.

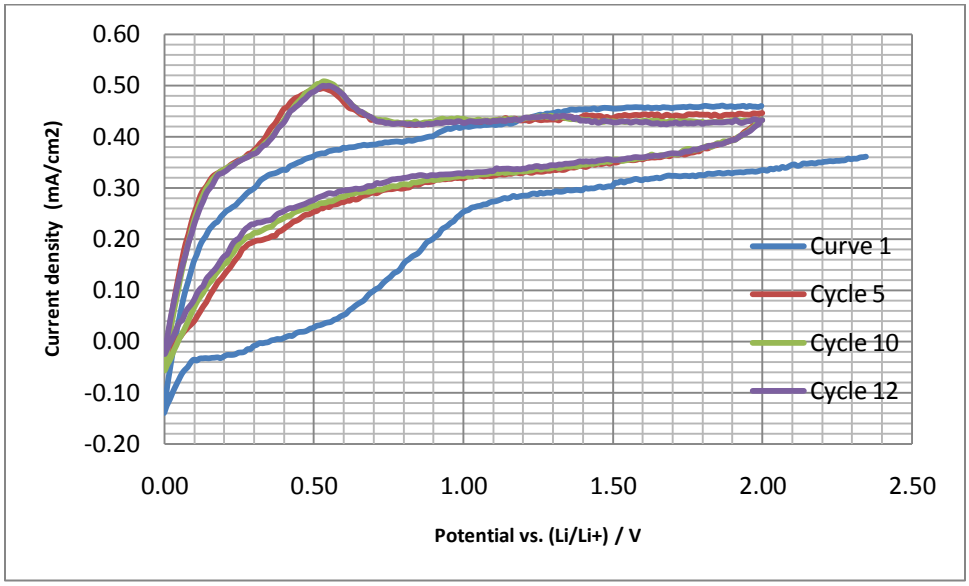

Figure 4.17 Cyclic voltammogram of PS as anode (copper on the backside of samples) in LIBs. Scan rate: 0.2mV/sec. The PS was fabricated under the condition of 40 minutes of anodization etching time, 4 M HF concentration and 40 mA/cm^2 current density.

From figure 4.17 is the cyclic voltammogram of the PS fabricated by 40 minutes of anodization etching. The reduction current density peaks are -0.14 mA/cm^2, -0.04 mA/cm^2, -0.06 mA/cm^2 and -0.02 mA/cm^2 at the first cycle, fifth cycle, 10th cycle and 12th cycle respectively. The oxidation current density peaks are 0.49mA/cm^2, 0.51 mA/cm^2, and 0.50 mA/cm^2 at fifth cycle, 10th cycle and 12th cycle respectively. The discharge and charge curve is stable from the cycle 5 to cycle 12, which indicates that lithium diffusion and electrochemical kinetics reach an optimal state.

The first broad reduction current peak during the first cycle may originate from the decomposition of CuO and formation of SEI films due to decomposition of

electrolyte on the film surface at the cycle 1 in figure 4.17, which disappear from the subsequent cycles.

4.3.7 Cyclic voltammograms with coated Pt on the backside of sample

The tested sample with Platinum on the backside showed the similar characteristics as the sample with gold on the backside mentioned in the section 4.3.1. Seen from the table 4.5, the reduction current density peaks (absolute value) of PS at 40 minutes of etching time is larger than the ones of flat silicon film, and the peak of current density increased with the pore depth at the scan rate 20mV/s, these characteristics demonstrated again that the depth of the pore is useful for the lithiation process, and part of the deep pore takes part in the lithiation and delithaition process.

Table 4.5 Comparison of the cyclic voltammograms by PS with different anodization etching time as anode in LIBs (Pt).

	Reduction current density peak at 5th cycle, rate 50mV/s (mA/cm2)	Reduction current density peak at 1st cycle, rate 20mV/s (mA/cm2)	Reduction current density peak at 2nd cycle, rate 20mV/s (mA/cm2)
Si	-0.55	-0.36	-0.30
PS 10mins	-0.70	-0.56	-0.52
PS 25mins	-0.53	-0.44	-0.42
PS 40mins	-1.45	-1.11	-0.98
PS 55mins	-0.48	-0.36	-0.31
PS 70mins	-0.44	-0.35	-0.33

4.4 Summary

In this chapter, the Li storage characteristics in PS were assessed electrochemically by using CV and galconostatic methods. The PS showed better electrochemical performance than flat Si. The depth of porous silicon was beneficial to improve the lithium storage capacity due to the enlarged contacted surface area. The agglomerates on surface were captured by SEM images, which enlarged the surface contacting with electrolyte and provided more surface area for lithiation process. The mass of PS excluding silicon substrate was calculated by OOF2 analysis, so the accurate capacity can be measured in the CV test. The free-standing PS without silicon substrate was determined by galvonostatic discharge and charge, which attained the 1150mAh/g of capacity.

From the table 4.6, the PS with coated Cu shows the highest reduction current density peaks, which indicates that Cu is most active material with Si.

Table 4.6 Comparison of the reduction current density peaks with different coated metal (Au, Cu and Pt) on the backside of PS samples, scan rate: 50mV/s, 5th cycle.

	Reduction current density with Au (mA/cm2)	Reduction current density with Cu (mA/cm2)	Reduction current density with Pt (mA/cm2)
Si	-0.56	-2.93	-0.55
PS 10mins	-1.24	-5.09	-0.70
PS 40mins	-1.39	-6.87	-1.45
PS 55mins	-1.76	-3.76	-0.48
PS 70mins	-1.30	-1.59	-0.44

Chapter 5 Conclusions and future works

5.1 Conclusions

The studies on porous silicon membranes for lithium-ion batteries anode applications were developed, demonstrated and characterized systematically in this work. The experimental results have displayed that the structured porous silicon can be produced in a relatively simple way by employing electrochemical anodization of single crystalline silicon wafer in a mixed solution of Dimethylformamide (DMF) and Hydrofluoric acid (HF wt.49%). Scanning Electron Microscopy (SEM) and Finite Element Analysis (OOF2) have been utilized to reveal the properties of the porous layer.

In general, the pore depth was enhanced with the etching time at a given current density. The etch rate of porous silicon at a given etching time increases with the current density. The **average** diameters of the pores are in the range between 0.85μm and 1.53μm.

Electrochemical measurements were conducted on both Si-wafer supported and free-standing porous Si membranes by cyclic voltammetry method (CV) and galvanostatic discharge/charge test. The Si-wafer supported PS anode showed high cycling stability, manifested by the unchanged porous structure after 10 charge-discharge cycles. Along with the increase of the depth of the pores, the specific capacity was increased due to the enlarged surface area. Specific capacity up to 1150mAh/g was achieved by free-standing porous Si membranes.

In this work, the change of the sidewall's surface morphology of the pores was observed after lithium insertion by SEM. It turned out that the silicon micro-structured membrane can incorporate large amount of Li atoms without fracturing, making it a promising candidate for the anode in Li ion batteries.

5.2 Future works

The free-standing porous Si membranes as anode in Lithium-ion batteries showed high Li-storage capacity in the first and second cycle, but larger capacity fading at successive cycles. The improvement in cycle life and capacity still need to be investigated.

Further research work should focus on free-standing PS membranes as anode in the following aspects,

1) Minimize the native silicon dioxide on the free-standing porous Si membranes.

The porous silicon is easy to be oxidized forming a silicon dioxide layer at ambient condition. The fabricated free-standing PS membranes should be prevented from the contact with air, sealed immediately after completing fabrication, and assembled in the glove box after being dried in a vacuum oven.

2) Identify the electrochemical agglomeration on pore wall.

The agglomeration on pore wall was observed in this work shown in figure 4.12. In future work, it should be clear that the agglomeration whether it is crystalline Si or amorphous Li-Si phases. Cui's group has observed both the crystalline core and an amorphous shell formed along the Si NW shown in the figure 5.1[33].

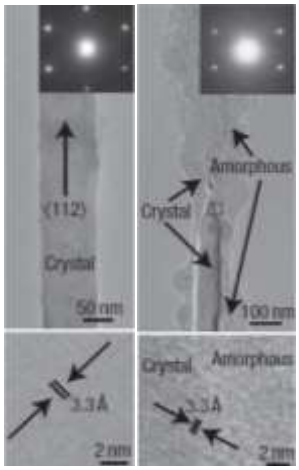

(a) (b)

Figure 5.1 Structural evolution of Si NWs during lithiation (a) single-crystalline Si NW before electrochemical cycling (b) crystalline core and the Li_xSi amorphous shell after electrochemical cycling[33].

3) Improve the delithiation process.

Xuejie Huang's group in China stated that the trapping of Li ions occurred and resulted in the capacity loss [35]. In future research work, the trapping of Li ions should be investigated during delithiation process, which should make sure whether the part of delithiation process is irreversible due to the formed amorphous Si. If the delithiation process is irreversible, maybe other materials should be added working as additive to improve the delithiation process.

4) Improve the contact between free-standing porous silicon and the current collector.

The free-standing PS membranes with coated Cu as anode were not completely investigated, so this part of data did not show up in this work. In future research work, the anode sample with coated Cu or other metal should be investigated, which will make sure whether the enforced conductivity will improve the performance of Lithium-ion batteries.

5) Reduce the stress and strain arising from volume expansion/contraction during cycling.

The structure of PS should be optimized to suit to volume expansion during lithium insertion/ removal of process.

6) Identify the SEI layer

The SEI layer which affected the performance of Lithium-ion batteries was not investigated in this work. Analysis of SEI can be undertaken for further investigation.

REFERENCES

[1] "EIA - International Energy Outlook 2008-World Energy Demand and Economic Outlook." Energy Information Administration - EIA - Official Energy Statistics from the U.S. Government. June 2008. 08 Apr. 2009 <http://www.eia.doe.gov/oiaf/ieo/world.html>.

[2] Chunhai Jiang, Eiji Hosono and Haoshen Zhou "Nanomaterials for lithium ion batteries" Nano Today, 1 (4), P 28-33, 2006.

[3] Goojin Jeong, Young-Ugk Kim, Hansu Kim, "Prospective materials and applications for Li secondary batteries", Energy Environ. Sci., 2011, 4, 1986-2002

[4] J.M. Tarascon, M. Armand, "Issues and challenges facing rechargeable lithium batteries", Nature 414, p359 (2001).

[5] G.M. Ehrlich, in David Linden (Ed.), Handbook of Batteries, 3rd ed., McGraw Hill, 2002.

[6] Rui Huang, Jing Zhu**,** "Silicon nanowire array films as advanced anode materials for lithium-ion batteries," Materials Chemistry and Physics Volume 121, Issue 3, P 519-522,2010.

[7] DeltaGray—Http://www.ctcms.nist.gov/~langer/oof2man/RegisteredClass-DeltaGray.html

[8] M Stanley Whittingham, "Electrochemical energy storage and intercalation chemistry", Science 192, 1226 (1976).

[9] C A Vincent, Modern batteries: An Introduction to Electrochemical Power Sources, 2nd ed., 1997.

[10] A. Manthiram, "Materials Challenges and Opportunities of Lithium-ion Batteries," Journal of Physical Chemistry Letters, 2, 176-184 (2011).

[11] Gholam-Abbas Nazri, Gianfranco Pistoia,Lithium-ion batteries science and technologies, Springer,2003.

[12] Ying Wang, Guozhong Cao, "Developments in Nanostructured Cathode Materials for High-Performance Lithium-Ion Batteries", Advanced Materials,Vol 20, 2251–2269, (2008).

[13]M. Stanley Whittingham, "Lithium Batteries and Cathode Materials", Chem. Rev., 104, 4271-4301,(2004).

[14] Hong Li, Zhaoxiang Wang, Liquan Chen, "Research on Advanced Materials for Li-ion Batteries", Adv. Mater., Vol 21, 4593–4607 (2009).

[15] "Lithium-ion battery", Http://en.wikipedia.org/wiki/Lithium-ion_battery#cite_note-13

[16] Wei-Jun Zhang, " A review of the electrochemical performance of alloy anodes for lithium-ion batteries", Journal of Power Sources 196, 13–24, (2011).

[17] Andrzej Lewandowski, Agnieszka Swiderska-Mocek, "Ionic liquids as electrolytes for Li-ion batteries—An overview of electrochemical studies", Journal of Power Sources, 194, 601–609, (2009).

[18] Masataka Wakihara, "Recent developments in lithium ion batteries", Materials Science and Engineering: R: Reports, Vol. 33, 109-134, (2001).

[19] A. Uhlir, "Electrolytic shaping of germanium and silicon", Bell Syst. Tech. J. 35, pp. 333–347, (1956).

[20] Y.T.Cheng and M.W.Verbrugge, "*Diffusion-Induced Stress*, *Interfacial Charge Transfer, and Criteria for Avoiding Crack Initiation of Electrode Particles,"* J. Electrochem. Soc., Volume 157, Issue 4, pp. A508-A516 (2010).

[21] A. K. Shukla, T. Prem Kumar, "Materials for next-generation lithium batteries", CURRENT SCIENCE, Vol. 94, 314-331, (2008).

[22] H. Okamoto, The Li-Si (Lithium-Silicon) System, Bull.Alloy Phase Diagrams, 11(3), p 306-312, (1990).

[23] Martin Winter, J.O.Besenhard, "Electrochemical lithiation of tin and tin-based intermetallics and composites", Electrochimica Acta, 45,31-50, (1999)

[24] Yoshio, M.; Tsumura, T.; Dimov, N. "Electrochemical behaviors of silicon based anode material", *J. Power Sources*. v. 146 , p. 10. 2005.

[25] M.N. Obrovac, L. Christensen, D.B. Le, J.R. Dahn, "Alloy Design for Lithium-Ion Battery Anodes",J. Electrochem. Soc. 154, A849, (2007).

[26] Jun Liu, Guozhong Cao, Zhenguo Yang, "Oriented Nanostructures for Energy Conversion and Storage", ChemSusChem, 1,676-697,(2008)

[27] Uday Kasavajjula, Chunsheng Wang a, A. John Appleby, " Nano- and bulk-silicon-based insertion anodes for lithium-ion secondary cells " Journal of Power Sources 163, 1003–1039 (2007) .

[28] B. A. Boukamp, G.C. Lesh and R. A. Huggins, “All-Solid Lithium Electrodes with Mixed-Conductor Matrix”, J. Electrochem. Soc. 128, 725 (1981).

[29] V.L. Chevrier, J.W. Zwanzigerb, J.R. Dahna, “First principles study of Li–Si crystalline phases Charge transfer, electronic”, Journal of Alloys and Compounds 496, 25–36, (2010)

[30] Arun Patil, Vaishali Patil, Dong Wook Shin, “Issue and challenges facing rechargeable thin film lithium batteries”, Materials Research Bulletin, 43 1913–1942, (2008).

[31] Yu-Guo Guo, Jin-Song Hu, and Li-Jun Wan, “Nanostructured Materials for Electrochemical Energy Conversion and Storage Devices”, Adv. Mater., 20, 2878–2887, (2008).

[32] A. Manthiram, A. Vadivel Murugan, A. Sarkar, “Nanostructured electrode materials for electrochemical energy storage and conversion”, Energy Environ. Sci., 1, 621–638, (2008).

[33] CANDACE K. CHAN, HAILIN PENG, GAO LIU, KEVIN McILWRATH, XIAO FENG ZHANG,ROBERT A. HUGGINS AND YI CUI, "High-performance lithium battery anodes using silicon nanowires," *Nature Nanotechnology* 3, 31 - 35 (2008) .

[34] Kuiqing Peng, Jiansheng Jie, Wenjun Zhang and Shuit-Tong Lee1, “Silicon nanowires for rechargeable lithium-ion battery anodes” APPLIED PHYSICS LETTERS 93, 033105 (2008).

[35] Hong Li, Lihong Shi, Qing Wang, Liquan Chen, Xuejie Huang, “Nano-alloy anode for lithium ion batteries”, Solid State Ionics, Vol 148, 247– 258, (2002).

[36] Park, M.-H., Kim, M. G., Joo, J., Kim, K., Kim, J., Ahn, S., Cui, Y.,“Silicon Nanotube Battery Anodes”, Nano Lett. 9, 3844–3847,(2009).

[37] H. C. Shin, J. A. Corno, J. L. Gole, and M. L. Liu, “Porous silicon negative electrodes for rechargeable lithium batteries”, J. Power Sources 139, 314 (2005).

[38] J.-H. Kwon, S.-H. Lee and B.-K. Ju, “Thin film silicon substrate formation using electrochemical anodic etching method”, Surface Engineering, VOL 25, (2009).

[39] H. Föll, M. Christophersen, J. Carstensen, G. Hasse, “Formation and application of porous silicon,” Materials Science and Engineering R 39, 93–141, (2002).

[40] Ralf B. Wehrspohn. in P.J. French and H. Ohji (Ed), Ordered Porous Nanostructures and Applications,Springer, 2005.

[41] Kurt petersen, "Silicon as a mechanical material", Proceedings of the IEEE, Vol. 70. No. 5, pp. 420-457, (1982).

[42] http://en.wikipedia.org/wiki/Silicon#cite_note-3

[43] Kittel C. Introduction to solid state physics (8th edition). New York: Wiley; 2004.

[44] G. Kovacs, Micromachined Transducers Sourcebook, McGraw-Hill, 1998

[45] Leigh Canham, Properties of porous silicon, Inspec, 1997.

[46] Volker Lehmann , Electrochemistry of Silicon Instrumentation: instrumentation, science, materials and applications, Wiley-VCH Verlag GmbH, 2002

[47] J. W. Gardner, V. K. Varadan, O. O. Awadelkarim, Microsensors, MEMS and Smart Devices, Wiley, 2001.

[48] M. Madou, Fundamentals of Microfabrication, CRC Press, 2nd ed., 2002.

[49] Sami Franssila, Introduction to Microfabrication, Wiley,2004.

[50] GREGORY T. A. KOVACS, "Bulk Micromachining of Silicon", PROCEEDINGS OF THE IEEE, VOL. 86, NO. 8, (1998).

[51] John J. Kelly, Harold G.G. Philipsen, "Anisotropy in the wet-etching of semiconductors", Current Opinion in Solid State and Materials Science, Vol 9, 84–90, (2005).

[52] Sebastian Patzig-Klein, GerhardRoewer,EdwinKroke, "New insights into acidic wet chemical silicon etching by HF/H_2O– $NOHSO_4$–H_2SO_4 solutions", Materials Science in Semiconductor Processing, 13, 71–79, (2010)

[53] R. L. Smith, S. D. Collins, "Porous silicon formation mechanisms" J. Appl. Phys. 71 (8), (1992).

[54] Lehmann V, Föll H, "Formation Mechanism and Properties of Electrochemically Etched Trenches in n-Type Silicon", J. Electrochem. Soc., Vol 137, 653, (1990).

[55] L. Pavesi, and V. Mulloni, "All porous silicon microcavities: growth and physics", J. Luminescence, 80, 43 (1999).

[56] E.K. Propst, P.A. Kohl, "The Electrochemical Oxidation of Silicon and Formation of Porous Silicon in Acetonitrile", J. Electrochem. Soc. 141, 1006-1013, (1994).

[57] E.A. PONOMAREV, C. LEVY-CL EMENT," Macropore Formation on p-Type Silicon", Journal of Porous Materials 7, 51–56, (2000).

[58] S. Lust, C. Lévy-Clément, "Macropore Formation on Medium Doped p-Type Silicon" physica status solidi (a) Volume 182, Issue 1, p17–21, November 2000.

[59] E.K. Propst and P.A. Kohl, "The electrochemical oxidation of silicon and formation of porous silicon in acetonitrile" J. Electrochem. Soc. 141, 1006–1013, (1994).

[60] V. Lehmann and S. Rönnebeck, "The Physics of Macropore Formation in Low-Doped p-. Type Silicon" J. Electrochem. Soc. 146 (8), 2968–2975 (1999).

[61] Vladimir Kochergin, Helmut Föll, Porous semiconductors: Optical properties and applications, Springer, 2009.

[62] Products: Celgard® Battery Separators, http://www.celgard.com/products/default.asp

[63] L. B. Chen, J. Y. Xie, H. C. Yu, T. H. Wang, "An amorphous Si thin film anode with high capacity and long cycling life for lithium ion batteries", J. Appl Electrochem., vol 39, 1157–1162, (2009).

Appendix

Table A.1 shows the summarized characteristics of PS including average diameter of pore, pore density, pore percentage, depth of pore and width of pore wall. As for the sample 1M01, because it is difficult distinguish between the pore and the wall, the calculation of average diameter of the pores, pore density N_p and average width of pore wall was not performed.

Table A.1 The characteristics of porous silicon

Etching time (mins)	HF concentration (M/L)	current density (mA/cm^2)	Sample	Average Diameter (μm)	Pore density N_p ($/\mu m^2$)	pore percentage	Width of pore wall (μm)
20	1	10	1M01	N/A	N/A	31.7%	N/A
		20	1M02	0.873	0.897	53.7%	0.183
		30	1M03	1.214	0.482	55.6%	0.229
	2	10	2M01	1.061	0.561	50.3%	0.273
		20	2M02	0.919	0.897	59.5%	0.136
		30	2M03	1.043	0.656	56.4%	0.195
	3	20	3M02	0.850	1.065	60.5%	0.119
		30	3M03	1.197	0.519	59.4%	0.189
	4	10	4M02	1.282	0.439	62.6%	0.228
		20	4M05	1.526	0.346	63.3%	0.174
		30	4M08	1.121	0.656	64.2%	0.114
		40	4M11	1.378	0.472	70.3%	0.078
30		40	4M12	0.832	1.292	70.2%	0.048

Table A.2 Top views of SEM image with the area percentage of pore calculation

1M01 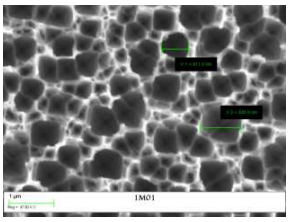 (a) 1023×680 pixels 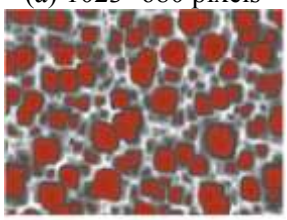 (b) 220842 pixels	**1M02** 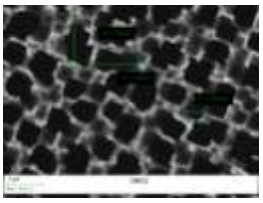 (a) 1022×674 pixels 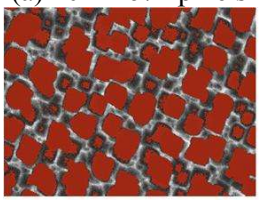 (b) 370049 pixels	**1M03** 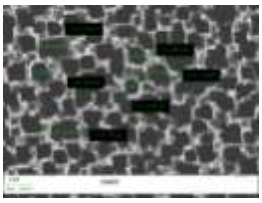 (a) 1023×672 pixels 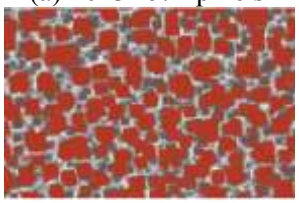 (b) 381917 pixels
2M01 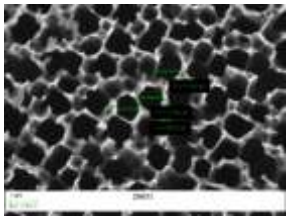 (a) 872×677 pixels 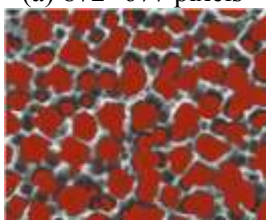 (b) 282418 pixels	**2M02** 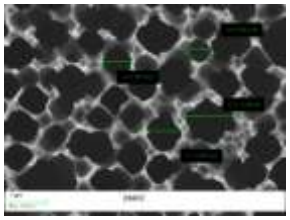 (a) 1016×671 pixels 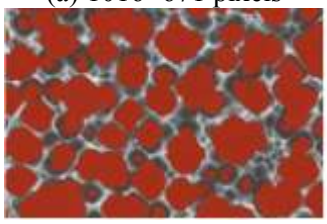 (b) 405346 pixels	**2M03** 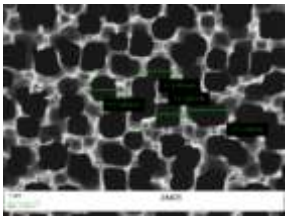 (a) 1023×674 pixels 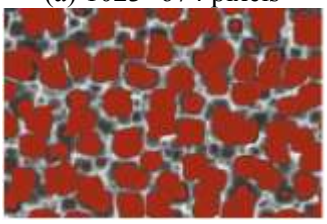 (b) 388655pixels
3M02 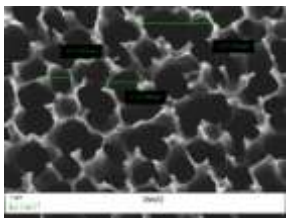 (a) 1020×674pixels 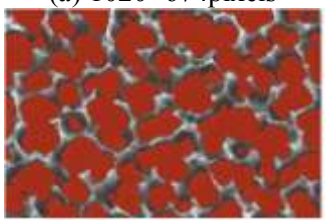 (b) 415594 pixels	**3M03** 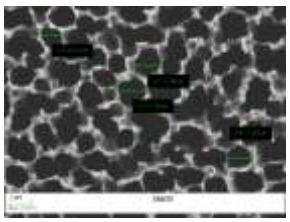 (a) 1023×677pixels 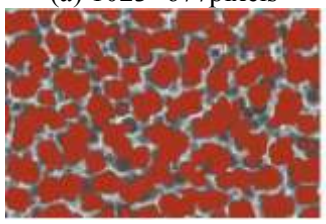 (b) 411221 pixels	**4M02** 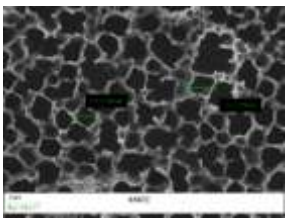 (a) 1008×667pixels 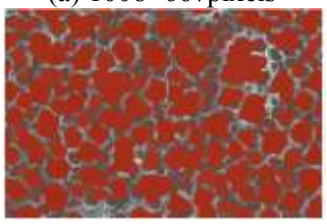 (b) 420762 pixels

4M05	4M08	4M11
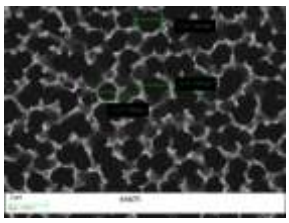 (a) 1018×667pixels	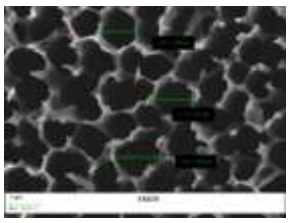 (a) 1019×665pixels	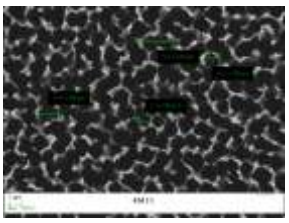 (a) 1024×672pixels
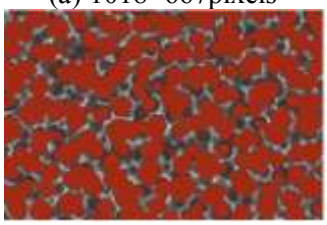 (b) 430149 pixels	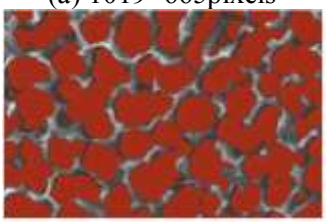 (b) 435225 pixels	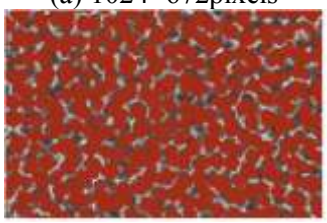 (b) 483536 pixels
4M12		
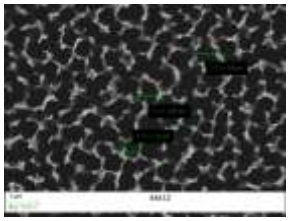 (a) 1015×672pixels		
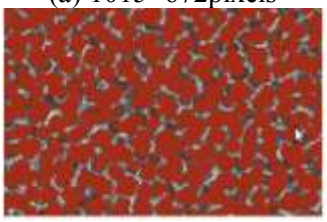 (b) 471664 pixels		

The pore diameter d, pore density N_p and width of pore's wall W are calculated by using OOF2 to discriminate the pore from the SEM image (table A.2). According to the different etching time, the depth of PS is shown in the table A.3.

Table A.3 Cross-sectional views of SEM images of PS with different HF concentration, current density and etching time.

4M01 4 M/L, 10 mA/cm^2, 10 mins	**4M02** 4 M/L, 10 mA/cm^2, 20 mins	**4M03** 4 M/L, 10 mA/cm^2, 30 mins
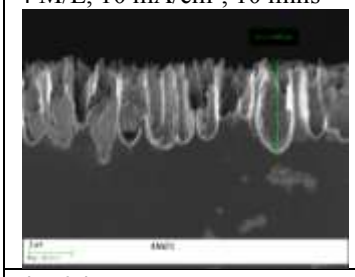	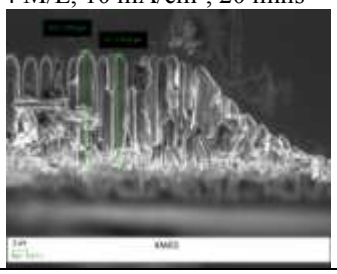	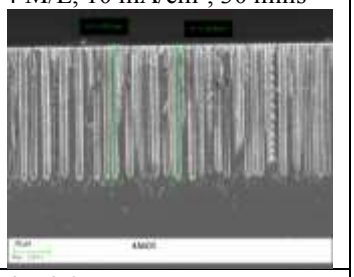
4M04 4 M/L, 20 mA/cm^2, 10 mins	**4M05** 4 M/L, 20 mA/cm^2, 20 mins	**4M06** 4 M/L, 20 mA/cm^2, 30 mins
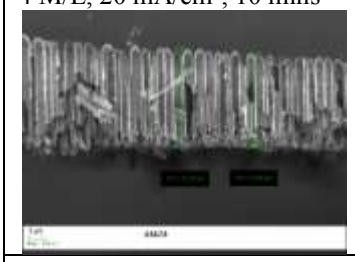	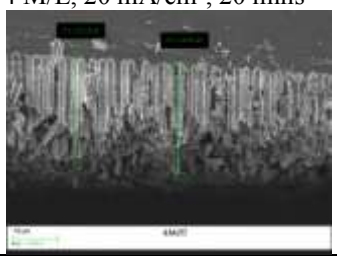	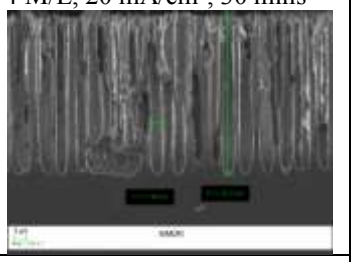
4M07 4 M/L, 30 mA/cm^2, 10 mins	**4M08** 4 M/L, 30 mA/cm^2, 20 mins	**4M09** 4 M/L, 30 mA/cm^2, 30 mins
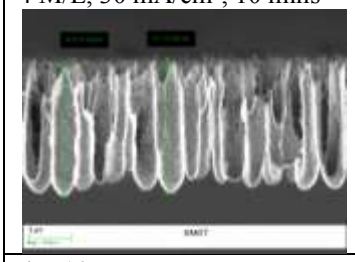	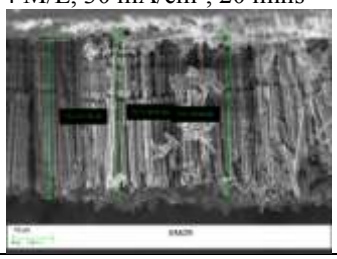	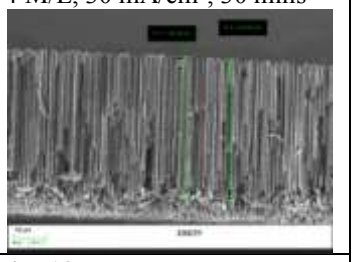
4M10 4 M/L, 40 mA/cm^2, 10 mins	**4M11** 4 M/L, 40 mA/cm^2, 20 mins	**4M12** 4 M/L, 40 mA/cm^2, 30 mins
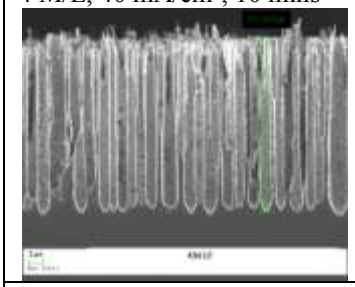	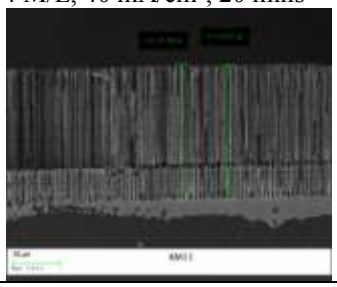	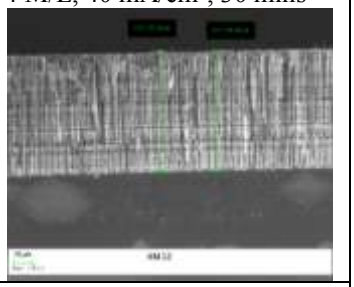
4M13 4 M/L, 40 mA/cm^2, 40 mins	**4M14** 4 M/L, 40 mA/cm^2, 55 mins	**4M15** 4 M/L, 40 mA/cm^2, 70 mins
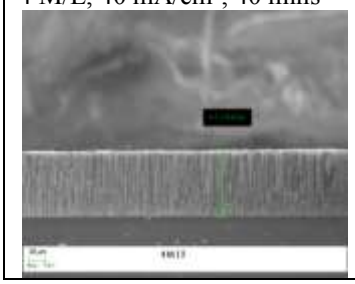	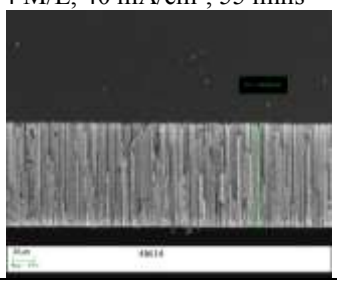	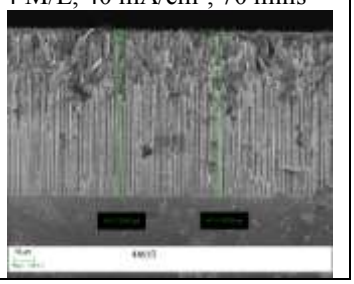

4M1016 Free-standing PS with evaporated Copper. 4 M/L, 50 mA/cm^2, 60 mins+ 10mins(with 32.1V) 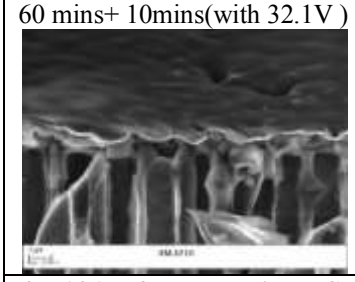	**4M1019** 4 M/L, 50 mA/cm^2, 30 mins 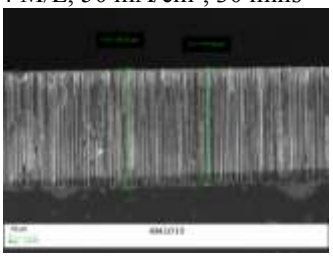	**4M1021** 4 M/L, 50 mA/cm^2, 60 mins 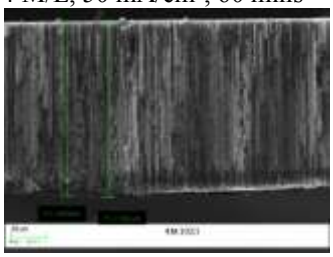
4M1017, free-standing PS 4 M/L, 50 mA/cm^2, 60 mins +15 mins (with 32.1V) 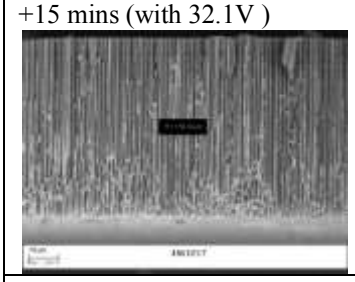	**3M01** 3 M/L, 10 mA/cm^2, 20 mins 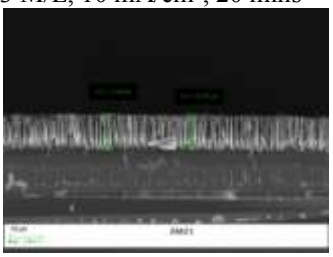	**3M02** 3 M/L, 20 mA/cm^2, 20 mins 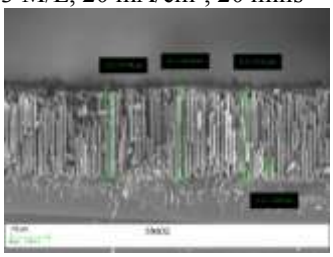
3M03 3 M/L, 30 mA/cm^2, 20 mins 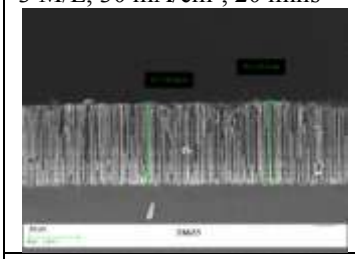	**2M01** 2 M/L, 10 mA/cm^2, 20 mins 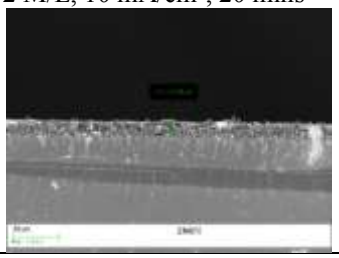	**2M02** 2 M/L, 20 mA/cm^2, 20 mins 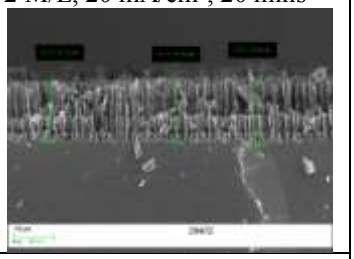
2M03 2 M/L, 30 mA/cm^2, 20 mins 	**1M01** 1 M/L, 10 mA/cm^2, 20 mins 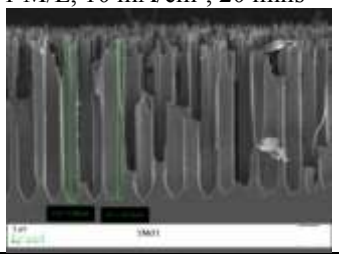	**1M02** 1 M/L, 20 mA/cm^2, 20 mins 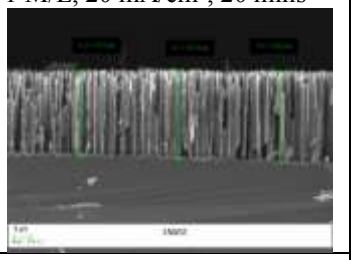
1M03 1 M/L, 30 mA/cm^2, 20 mins